

An Improved Double-Gaussian Closure for the Subgrid Vertical Velocity Probability Distribution Function

A. C. FITCH

Department of Meteorology, Stockholm University, Stockholm, Sweden, and Pacific Northwest National Laboratory, Richland, Washington, and Bolin Centre for Climate Research, Stockholm, Sweden

(Manuscript received 29 May 2018, in final form 24 September 2018)

ABSTRACT


The vertical velocity probability distribution function (PDF) is analyzed throughout the depth of the lower atmosphere, including the subcloud and cloud layers, in four large-eddy simulation (LES) cases of shallow cumulus and stratocumulus. Double-Gaussian PDF closures are examined to test their ability to represent a wide range of turbulence statistics, from stratocumulus cloud layers characterized by Gaussian turbulence to shallow cumulus cloud layers displaying strongly non-Gaussian turbulence statistics. While the majority of the model closures are found to perform well in the former case, the latter presents a considerable challenge. A new model closure is suggested that accounts for high skewness and kurtosis seen in shallow cumulus cloud layers. The well-established parabolic relationship between skewness and kurtosis is examined, with results in agreement with previous studies for the subcloud layer. In cumulus cloud layers, however, a modified relationship is necessary to improve performance. The new closure significantly improves the estimation of the vertical velocity PDF for shallow cumulus cloud layers, in addition to performing well for stratocumulus. In particular, the long updraft tail representing the bulk of cloudy points is much better represented and higher-order moments diagnosed from the PDF are also greatly improved. However, some deficiencies remain owing to fundamental limitations of representing highly non-Gaussian turbulence statistics with a double-Gaussian PDF.

1. Introduction

Turbulent vertical velocity fluctuations play a key role in planetary boundary layer (PBL) and cloud processes, and their representation forms a critical component of weather, climate, and dispersion models. One of the primary mechanisms for vertical transport of heat, moisture, momentum, and trace gases in the atmosphere is through turbulent eddies. For the scales at which most regional and global models operate, turbulent eddies are not resolved and must therefore be parameterized. At typical model gridbox sizes greater than $\sim 1\text{--}2$ km, the mean vertical velocity of all the updrafts and downdrafts contained within a grid box will be close to zero. However, in order to represent vertical transport and cloud processes correctly in models, it is critical to know how the vertical velocity is partitioned between updrafts and downdrafts within a grid box.

A key control in the formation of cloud droplets is the updraft velocity. The rate at which an air parcel rises controls its cooling and in turn supersaturation and activation of aerosol particles into droplets. A cloud droplet will continue to grow while the supersaturation in a rising, cooling air parcel exceeds the critical supersaturation. The number and size of cloud droplets are fundamental to the optical properties of clouds, as well as for precipitation—the so-called aerosol indirect effects (AIE). These effects constitute one of the greatest sources of uncertainty in modeling climate. Thus, a key to improving the simulation of clouds—and climate more generally—is an improved representation of the subgrid vertical velocity (Lohmann et al. 1999; Donner et al. 2016).

The distribution of subgrid vertical velocity may be incorporated indirectly, such as in mass-flux cumulus models, where the mass flux is the product of vertical velocity, density, and updraft area. Alternatively, the distribution of subgrid vertical velocity may be represented directly, using the approach of assumed probability distribution functions (PDFs). Initially, PDF methods involved only thermodynamic variables, such as temperature and moisture

 Denotes content that is immediately available upon publication as open access.

Corresponding author: A. C. Fitch, a.c.fitch@outlook.com

DOI: 10.1175/JAS-D-18-0149.1

© 2019 American Meteorological Society. For information regarding reuse of this content and general copyright information, consult the [AMS Copyright Policy](https://www.ametsoc.org/PUBSReuseLicenses) (www.ametsoc.org/PUBSReuseLicenses).

(Sommeria and Deardorff 1977; Mellor 1977), and later incorporated vertical velocity (Randall 1987; Lewellen and Yoh 1993, hereafter LY; Lappen and Randall 2001; Larson et al. 2002; Cheng and Xu 2008; Bogenschutz et al. 2012) to account for cloud dynamics. Some approaches represent the joint PDF, including vertical velocity, as a double-delta function (Randall 1987; Randall et al. 1992; Lappen and Randall 2001). However, owing to difficulties representing the skewed nature of the PDF in cumulus cloud layers with a double-delta function, subsequent approaches have used a double-Gaussian PDF (LY; Larson et al. 2002; Cheng and Xu 2008; Bogenschutz et al. 2012). The double-Gaussian PDF is one of the simplest distributions that will permit both symmetrical and skewed shapes, corresponding to Gaussian and non-Gaussian turbulence statistics, respectively. The ability to represent both regimes in a model is important, as they both occur frequently in the atmosphere.

Stratocumulus clouds typically exhibit Gaussian-like PDFs, whereas cumulus cloud layers with low-cloud fraction (less than $\sim 20\%$) may be strongly skewed and non-Gaussian. Observations of the vertical velocity PDF in convective boundary layers (CBLs) have shown it is generally positively skewed, with a negative mode (Berg et al. 2017). The shape of the PDF is a result of how the turbulence is typically organized in the CBL: strong updrafts occupying a small horizontal area embedded in subsidence (downdraft) regions with smaller velocities that occupy a larger horizontal area.

Direct representation of the vertical velocity PDF has a longer history in modeling of pollutant dispersion using Lagrangian stochastic models, where Barentsen and Berkowicz (1984) proposed using a double-Gaussian function to model the PDF of vertical velocity in the CBL. This model was later supported by observations in the PBL (Quintarelli 1990; Du et al. 1994). The means and relative amplitudes of the two Gaussians can vary, which allows a skewed distribution. If the two Gaussians overlap, then the PDF reduces to a single Gaussian. For cumulus, the main mode corresponds to mostly non-cloudy downdrafts, while the second mode corresponds to mostly narrow cloudy updrafts. To specify the double-Gaussian PDF, five parameters are required, corresponding to the relative amplitude, and the means and standard deviations of each Gaussian. If a model can predict the first five statistical moments of vertical velocity, then the PDF may be immediately specified. However, computing the higher-order moments is a difficult problem and expensive computationally. Thus, one or more closure assumptions are usually made to reduce the number of required moments.

To account for the skewness of the vertical velocity distribution, a model must be able to provide moments of

up to at least third order. Observations of higher-order vertical velocity turbulence statistics (moments greater than 2) in the atmosphere are difficult to obtain, as a long averaging period is required to reduce systematic measurement bias and to reach an acceptable level of accuracy. For this reason there are few observations of higher-order moments reported in the literature. Most observations have also been limited to the subcloud layer or the lowermost layers of cloud (e.g., Hogan et al. 2009; Ansmann et al. 2010; Lenschow et al. 2012; Tonttila et al. 2015; Maurer et al. 2016; Berg et al. 2017). One of the few studies to observe the vertical velocity structure throughout the full layer of cloud is from Ghate et al. (2014). However, they did not analyze the PDF.

Owing to the lack of data, direct numerical simulation (DNS) and LES studies have been used to provide further insight, for example, Moeng and Rotunno (1990), Lenschow et al. (2012), and Waggy et al. (2016). Again, these studies were limited to the subcloud layer, although Guo et al. (2008) compared LES and observations of higher-order vertical velocity statistics within a marine stratocumulus cloud layer. Moyer and Young (1991) and Ching et al. (2010) observed vertical velocity skewness within a marine stratocumulus cloud but did not look at the PDF. Larson et al. (2002) compared their parameterized vertical velocity PDF with airborne observations within stratocumulus and cumulus clouds, although only at a single level. Chu et al. (1996) and Liu et al. (2011) examined the vertical velocity PDF from observations and compared them with several parameterizations; however, their analysis was limited to the surface layer.

The aim of the present work is to examine the vertical velocity PDF throughout the depth of the lower atmosphere, including the cloud layer and above. To our knowledge this is the first study to do so. Several existing schemes to model the vertical velocity PDF are compared with LESs of neutral and unstably stratified boundary layers, topped by stratocumulus and shallow cumulus cloud layers, respectively. These schemes are now in use in some major climate models, for example, CESM (<http://www.cesm.ucar.edu>) and the Energy Exascale Earth System Model (E3SM) (<http://e3sm.org>). A new closure is suggested that improves performance within the cloud layer, where higher-order vertical velocity turbulence statistics are found to be markedly different from the subcloud layer.

The paper is organized as follows. Section 2 introduces the LES cases and model configuration. Section 3 examines vertical velocity statistics from the LES and compares them with observations and intercomparison model results, where available. Sections 4 and 5 discuss double-Gaussian PDF closures for vertical velocity, and examine the parabolic relationship between skewness

and kurtosis. A new closure is also introduced. Section 6 shows the resulting vertical velocity PDF within the cloud layer for the different model closures. Section 7 examines the updraft probability estimated by the different model closures, and section 8 presents results using the double-Gaussian PDFs to close higher-order moments.

2. Large-eddy simulations

We analyze the vertical velocity (w) PDF in four boundary layer cloud cases using LES. The Advanced Research version of WRF (WRF-ARW), versions 3.6 and 3.8.1, is run in LES mode using the WRF LES package released by Takanobu Yamaguchi (Yamaguchi and Feingold 2012; available at <http://esrl.noaa.gov/csd/staff/tak.yamaguchi/code/>) and updated to WRF, version 3.6 and 3.8.1, by the author (version 3.6 available from the same location). WRF is a nonhydrostatic fully compressible model and uses the covariant velocities (u, v, w), dry air mass, geopotential, potential temperature θ , and subgrid-scale (SGS) turbulent kinetic energy (TKE) as the basic prognostic variables (Yamaguchi and Feingold 2012). Sensitivity to the acoustic time step is found using potential temperature as a prognostic variable, which is remedied by instead using the moist potential temperature in version 3.8.1 simulations (Xiao et al. 2015). SGS turbulence is parameterized with a 1.5-order TKE closure (Klemp and Wilhelmson 1978; Deardorff 1980) and surface fluxes are computed using Monin–Obukhov similarity. For microphysics, this study uses the Morrison (Morrison et al. 2009) scheme, which prognoses mass mixing ratios of nonprecipitating water (vapor, water, and ice) and precipitating water (rain, snow, and graupel). Here, diagnosed number concentrations are used. The lateral boundary conditions are periodic and the upper boundary is rigid. A Rayleigh relaxation layer controls gravity wave reflection from the upper boundary.

A wide range of boundary layer cloud cases are examined: two marine shallow cumulus cases, a continental shallow cumulus case, and a marine stratocumulus case. The first is based on the Barbados Oceanographic and Meteorological Experiment (BOMEX) (Holland and Rasmusson 1973) and is a case of nonprecipitating trade wind cumulus. It is run using the same configuration as the Global Energy and Water Cycle Exchanges project (GEWEX) Global Atmospheric System Studies (GASS) (formerly GEWEX Cloud System Studies) intercomparison case (Siebesma et al. 2003). However, here the size of the domain is increased to $16.9\text{ km} \times 16.9\text{ km}$ with the model top at 7480 m to increase the turbulence statistics collected. The simulation is run using WRF, version 3.8.1, with horizontal and vertical resolutions of 100 and 40 m, respectively, and a

1-s time step. The case is run for 6 h, with results shown averaged over the last 3 h.

The second case is from the Rain in Cumulus over the Ocean (RICO) field campaign (Rauber et al. 2007) and is a precipitating trade wind cumulus case. It is run using the same configuration as the GASS intercomparison case (VanZanten et al. 2011). The simulation is run using WRF, version 3.6, with a horizontal and vertical resolution of 100 and 40 m, respectively, and a 1-s time step. The domain size is $12.9\text{ km} \times 12.9\text{ km}$ with the model top at 4000 m. The acoustic time step is set to 0.125 s. The cloud droplet number concentration is prescribed at 70 cm^{-3} . The case is run for 24 h, with results shown averaged over the last 4 h.

The third case is of nonprecipitating continental shallow cumulus and is based on observations made at the Southern Great Plains (SGP) site of the Atmospheric Radiation Measurement (ARM) program. The same configuration as for the GASS intercomparison is used (Brown et al. 2002). The simulation is run using WRF, version 3.8.1, with horizontal and vertical resolutions of 66.7 and 40 m, respectively, and a 0.5-s time step. The domain size is $6470\text{ m} \times 6470\text{ m}$ with the model top at 4400 m. The case is run for 14.5 h, with results shown averaged over 8.5–10.5 h, corresponding to 1400–1600 local time (LT).

The final and fourth case is from the first research flight (RF01) of the Second Dynamics and Chemistry of Marine Stratocumulus field study (DYCOMS-II) (Stevens et al. 2003) and is a marine stratocumulus case. Again, the same configuration as for the GASS intercomparison is used (Stevens et al. 2005). The simulation is run using WRF, version 3.6, with horizontal and vertical resolutions of 35 and 5 m, respectively, and a 0.1-s time step. The domain size is $3395\text{ m} \times 3395\text{ m}$ with the model top at 1500 m. The acoustic time step is set to 0.01 s. To maintain the cloud deck over time in line with the intercomparison models, the cloud droplet number concentration is prescribed at 120 cm^{-3} . The case is run for 4 h and the results shown are averaged over the last hour.

The sensitivity of higher-order moments of vertical velocity to the model resolution was examined in BOMEX and ARM, representing two very different shallow cumulus cases displaying strongly non-Gaussian turbulence statistics. In simulations doubling both the vertical and horizontal resolutions, differences in peak kurtosis in the cloud layer were found to be at most 2% for BOMEX and 18% for ARM. The sensitivity to resolution was not examined for DYCOMS RF01, as the high resolution of the standard intercomparison case was found to compare well with observations, and higher-order moments are of less interest for this case relative to the shallow cumulus cases.

For all simulations, the instantaneous three-dimensional vertical velocity field is saved every 5 min of simulation. The results shown are averaged from this output.

3. Vertical velocity statistics

The turbulent structure of the PBL is reflected in the vertical velocity statistical moments. The variance, $\sigma_w^2 = \overline{w^2}$, is a measure of the intensity of turbulence, and higher-order moments (>2) indicate the turbulence organization. The skewness, $S = \overline{w^3}/\overline{w^2}^{3/2}$, a normalized measure of the third moment $\overline{w^3}$, indicates the relative frequency of extreme values of the vertical velocity. Small values of S and $\overline{w^3}$ occur when the distribution is relatively symmetric between updrafts and downdrafts. A positive value indicates strong and narrow updrafts are more likely to occur than strong and narrow downdrafts. A negative value reflects stronger and narrow downdrafts. The kurtosis, $K = \overline{w^4}/\overline{w^2}^2$, a normalized measure of the fourth moment $\overline{w^4}$, also indicates the frequency at which extreme values of vertical velocity occur. A kurtosis greater than the value for a Gaussian distribution, that is, 3, indicates an increase in extreme values together with a high probability of small values about the mean, with respect to a Gaussian distribution.

The mean profiles of vertical velocity variance, skewness, and kurtosis are shown in Figs. 1 and 2 for each case. For DYCOMS RF01, a maximum in the vertical velocity variance is seen around cloud base (Fig. 1a). The simulation is more energetic than most of the intercomparison models throughout most of the PBL and is much closer to observations than the intercomparison mean. Observations of the third moment (Fig. 1b) show negative values throughout most of the cloud layer and in the upper subcloud layer, reflecting strong downdrafts driven by cloud-top radiative cooling, which are typical for a stratocumulus cloud. Again, the simulation results are much closer to the observations than the intercomparison mean, which displays the wrong sign throughout most of the PBL. The latter is indicative of decoupling, where the turbulence has become more surface driven, resulting in positive values of the third moment. The skewness in the simulation (Fig. 1c) reflects similar properties as the third moment. Comparatively small values are seen relative to the shallow cumulus cases, indicative of largely symmetric, Gaussian turbulence. A maximum in skewness is seen at cloud top. Model intercomparison and observational data are not available for the skewness for this case. The kurtosis (Fig. 1d) displays largely Gaussian values (around 3), apart from a sharp peak at cloud top. Similar to the skewness, this indicates mostly symmetric, Gaussian turbulence. Observational or model intercomparison data are not available for the kurtosis for any of the cases.

For the BOMEX shallow cumulus case, the vertical velocity variance (Fig. 2a) shows a peak around the middle of the subcloud layer, a minimum around cloud base, and a second peak in the cloud layer. The peak in the subcloud layer is due to surface fluxes, whereas the peak in the cloud layer is related to enhanced turbulence from latent heat release. The simulation here is somewhat more energetic than the intercomparison cases in the upper subcloud layer and lower cloud layer. The peak in the cloud layer is about the same as the intercomparison mean. There are no observations for comparison in this case. The skewness (Fig. 2b) is positive throughout the PBL (apart from some small negative values in the upper cloud layer), indicative of stronger updrafts. The skewness increases through the cloud layer to reach a maximum value of around 3 near the center of the cloud. The increase in skewness reflects updrafts becoming stronger and narrower with height. There are no intercomparison or observational data available for the skewness. The kurtosis for this case (Fig. 2c) exhibits Gaussian values near the surface and above the cloud layer. It gradually increases away from the surface in the subcloud layer, in line with previous observations in the CBL, for example, Lenschow et al. (2012). Values of around 6 are seen just below cloud base. Above this, the kurtosis increases sharply within the cloud layer to reach a maximum of around 48 near the center. Few reports exist on the vertical velocity kurtosis within shallow cumulus, although large values in the center of the cloud layer are also found in the LES performed by Zhu and Zuidema (2009, their Fig. 3). A similar kurtosis profile within a shallow cumulus cloud is seen in Fig. 13 of Bougeault (1981) in his numerical simulation, although with a lower peak value of around 16. The high kurtosis is a result of low-cloud fraction typical of shallow cumulus, with predominantly small fluctuations about the mean in clear air, coupled with strong, narrow updrafts in cloudy air that form the long tail in the vertical velocity distribution. There are no observational data for comparison for this case.

The RICO shallow cumulus case shows overall qualitatively similar vertical velocity statistics as the BOMEX case (Figs. 2d–f). There is again a double peak in the variance, with the simulation here more energetic than the intercomparison models. This case is more energetic in the cloud layer than the BOMEX case. The skewness is mostly close to the intercomparison mean and peaks in the center of the cloud layer around 3, similar to BOMEX, although it decreases less rapidly around the peak. The kurtosis is mostly close to Gaussian in the subcloud layer and above the cloud, and increases with height in the subcloud layer. It peaks around 38 in the center of the

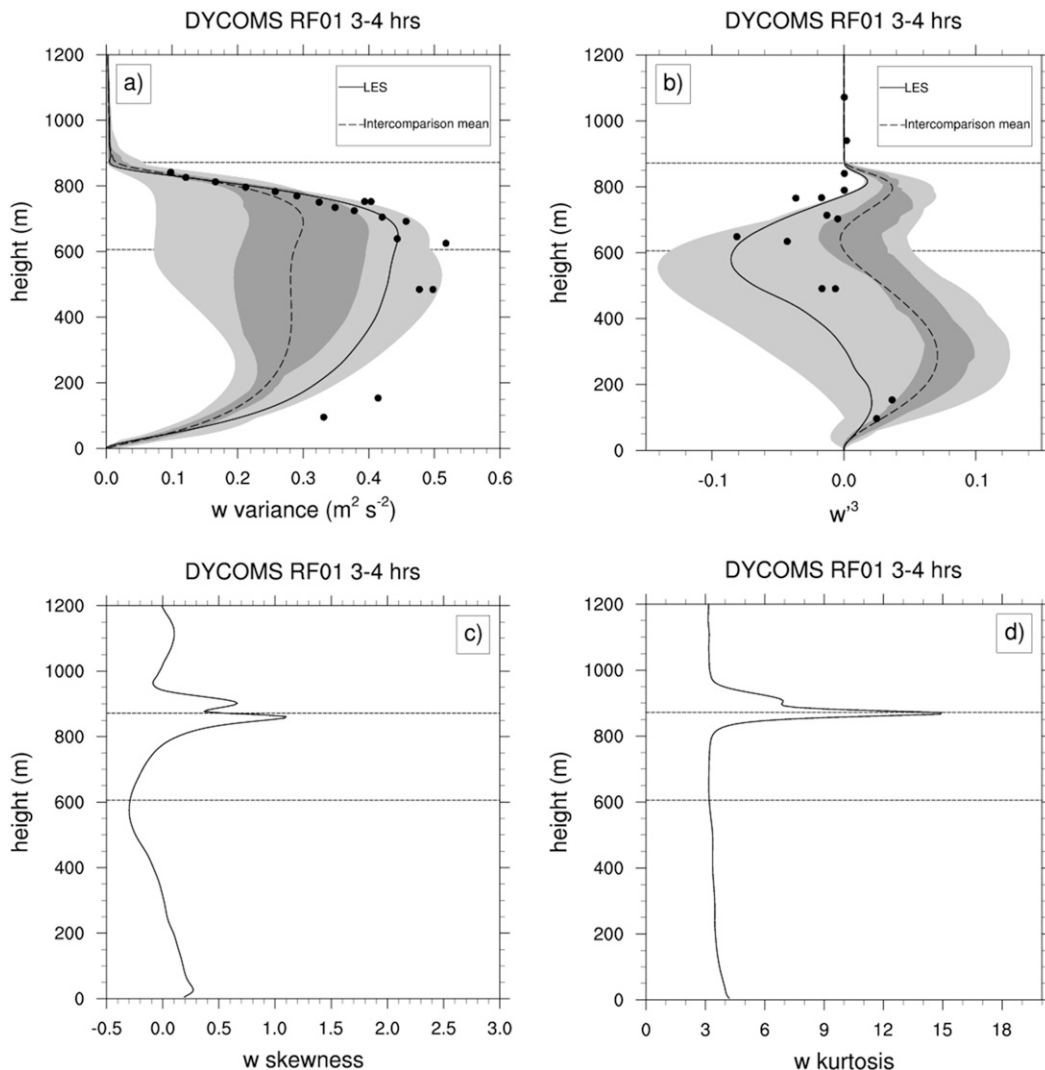


FIG. 1. Vertical mean profiles from LES for the DYCOMS RF01 case for (a) variance of w , (b) third moment of w , (c) skewness of w , and (d) kurtosis of w . Horizontal dashed lines indicate the cloud layer, defined as any point with $q_l > 0$. LES model intercomparison results are shown in (a) and (b), with light gray shading the minimum and maximum range and dark gray shading the interquartile range. Also, observations are shown with black circles (Stevens et al. 2005), the solid black line is the LES result from this study, and the dashed black line is the mean of the intercomparison models.

cloud layer. There are no observational data for comparison for this case.

The ARM case differs from the other shallow cumulus cases in that it is driven by stronger surface fluxes over land. More energetic turbulent eddies result, reflected in the vertical velocity variance profile (Fig. 2g). Higher values are seen in both the subcloud and cloud layers relative to the other cases. The skewness (Fig. 2h) for this case does not exhibit the same well-defined peaks as for BOMEX and RICO in the cloud layer and varies more gradually. A maximum skewness of around 1.2 is seen at the top of the subcloud layer and in the center of

the cloud layer. The kurtosis (Fig. 2i) peaks at the top of the cloud layer, unlike BOMEX and RICO, which peak closer to the center of the cloud. The kurtosis reaches a maximum of about 40 for ARM.

4. Modeling the vertical velocity PDF

If a model was able to predict an infinite number of statistical moments, then the vertical velocity PDF could be exactly defined (Shohat and Tamarkin 1943). However, owing to computational expense, only a very limited number may be predicted. Thus, any relationships

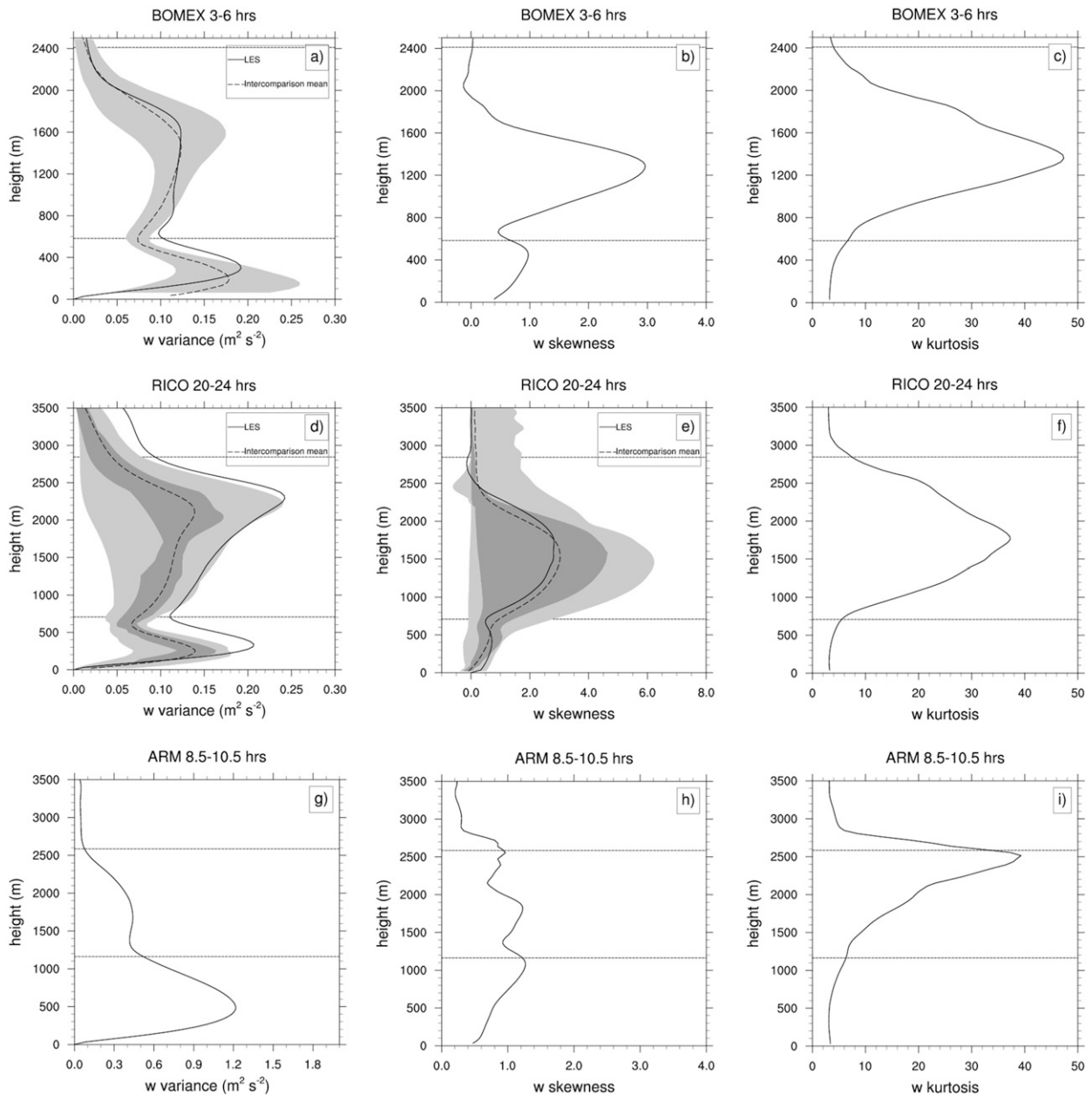


FIG. 2. As in Fig. 1, but with the LES results for the (a)–(c) BOMEX, (d)–(f) RICO, and (g)–(i) ARM cases. (left) The variance of w , (center) the skewness of w , and (right) the kurtosis of w .

between moments that can be used to diagnose higher-order moments not predicted by the model are very beneficial. Most atmospheric models in current use predict up to the third-order moments at most. However, this leaves the fourth-order moments that still need to be diagnosed to close the third-order moment equations. The earliest approaches used the Millionshchikov hypothesis (Millionshchikov 1941; Monin and Yaglom 1971, 1975), which states that the fourth-order moments can be assumed to be quasi normal (Gaussian). This

assumption has been used in many models (e.g., André et al. 1976; Moeng and Randall (1984); Canuto et al. (1994). However, subsequent studies have found this assumption to fail for skewed convective boundary layers (Ilyushin and Kurbatskii 1997; Canuto et al. 2001; Gryanik and Hartmann 2002, hereafter GH; Alberghi et al. 2002). The results shown in Fig. 2 for the shallow cumulus cases corroborate these studies, where the fourth-order vertical velocity moments are very large and far from Gaussian. Prior studies have been limited to

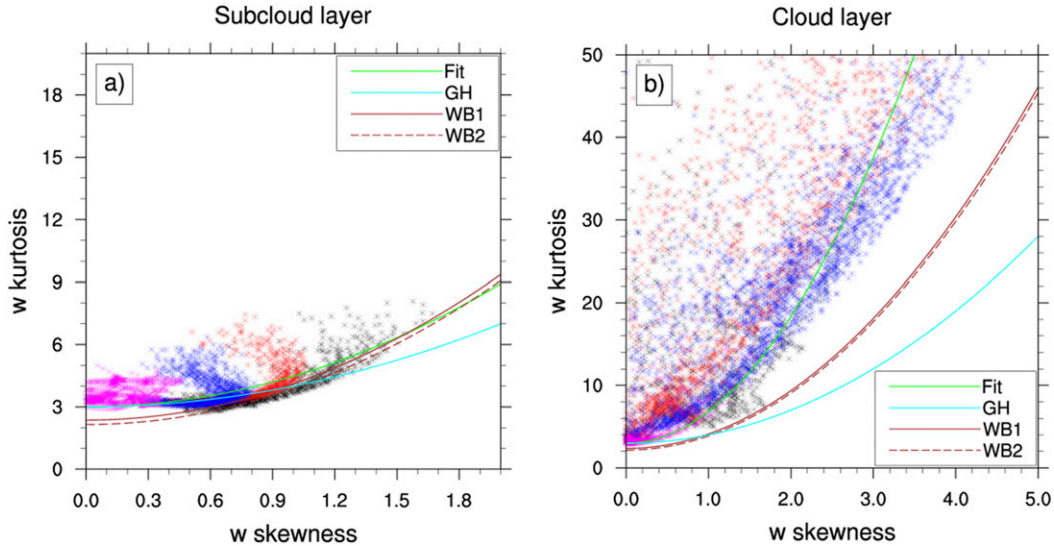


FIG. 3. The relationship between skewness and kurtosis for every LES grid point over the time period specified in section 2, for (a) points within the subcloud layer and (b) points within the cloud layer. Results for BOMEX, RICO, ARM and DYCOMS RF01 are shown in red, blue, black, and magenta, respectively. The green curve shows the best fit to the LES, while the other curves are previously suggested relations discussed in the text.

the subcloud layer, and one of the aims of the present work is to examine fourth-order closures for the entire depth of the lower atmosphere, including the cloud layer. As we have seen in Fig. 2, extreme departures from Gaussian values are seen for the kurtosis (normalized fourth-order moment) in the shallow cumulus cloud layer.

A parabolic relationship between skewness and kurtosis has been found, which can be used to define fourth-order closures. Such a relationship exists not only for atmospheric turbulence but also for other complex dynamical systems in fields as diverse as plasma physics and financial markets (Cristelli et al. 2012). The first was proposed by Mole and Clarke (1995) for atmospheric diffusion,

$$K = aS^2 + b, \tag{1}$$

where S is the skewness, K is the kurtosis, and a and b are constants.

Tampieri et al. (2000) proposed $a = b = 3.3$ for the vertical velocity of purely shear-driven turbulence. Waggy et al. (2016) found $a = b = 2.7$ gave a better fit for the neutral PBL in their DNS, which is in agreement with $a = b = 2.4 \pm 0.3$ from Alberghi et al. (2002) for observations in the CBL. GH argued that as S approaches zero, the fourth-order moments should approach Gaussian values. This assumption implies $a = 1$ and $b = 3$. The results of Waggy et al. (2016) were in agreement. The closure of GH is designed to be universal, in that it describes Gaussian turbulence in the limit of small skewness and strongly non-Gaussian skewed turbulence in the limit of large skewness.

Figure 3a shows the relationship between S and K for all the LES cases, for points within the subcloud layer for the time periods specified in section 2 for each case. The best nonlinear least squares fit for the LES data (with the constraint when $S = 0$ and $K = 3$) is shown by the green curve, with constants $a = 1.48$ and $b = 3.0$. This curve provides a reasonable fit to the data for all cases, although points approaching the cloud layer deviate more, displaying greater kurtosis. The relationship from GH, shown by the blue curve, also provides a reasonable fit to the LES data. The curves from the B1 and B2 experiments (shown by the brown solid and dashed lines, respectively, in Fig. 3) from Waggy et al. (2016) agree well for $S > \sim 0.6$, although below this value the kurtosis is underestimated.

Within the cloud layer (Fig. 3b), however, the kurtosis increases more rapidly with skewness than in the subcloud layer and the aforementioned relationships break down. The different behavior in the cloud layer is due to enhanced turbulence from latent heat release. The best nonlinear least squares fit to the LES data (with the constraint when $S = 0$ and $K = 3$) within the cloud layer is shown by the green curve in Fig. 2b, with constants $a = 3.84$ and $b = 3.0$.

Overall, the following relationships between skewness and kurtosis are found to give the best fit to the LES data:

$$K = \begin{cases} 3.84S^2 + 3, & \text{in cloud layer} \\ 1.48S^2 + 3, & \text{otherwise,} \end{cases} \tag{2}$$

where the cloud layer is defined here as any level in the LES where the mean liquid water mixing ratio q_l is greater than zero. If no information is available regarding the cloud layer, then the following relationships depending only on S are found to give a reasonable fit to the LES data (discussed in the next section):

$$K = \begin{cases} 1.48S^2 + 3, & \text{if } S < 1.4 \\ 3.84S^2 + 3, & \text{if } S \geq 1.4 \end{cases} \quad (3)$$

The new relationships will subsequently be used to diagnose the kurtosis from the skewness, in both the subcloud and cloud layers, and to define a closure for specifying the double-Gaussian PDF parameters for vertical velocity, discussed in the next section.

5. Specifying double-Gaussian PDF parameters

The double-Gaussian PDF is defined by five parameters: the relative amplitude a , the means w_1 and w_2 , and the standard deviations σ_1 and σ_2 of Gaussians 1 and 2, respectively. Here, a is defined as the amplitude of the Gaussian with the largest amplitude, named Gaussian 1. The method of moments can be used to define the PDF parameters, where the PDF moments are chosen to match model-predicted statistical moments of vertical velocity. The first three moments of the double-Gaussian vertical velocity PDF, obtained by integrating the moments over the double-Gaussian PDF, are

$$\bar{w} = aw_1 + (1-a)w_2, \quad (4)$$

$$\begin{aligned} \overline{w^2} &= a \left[(w_1 - \bar{w})^2 + \sigma_1^2 \right] \\ &+ (1-a) \left[(w_2 - \bar{w})^2 + \sigma_2^2 \right], \end{aligned} \quad (5)$$

and

$$\begin{aligned} \overline{w^3} &= a \left[(w_1 - \bar{w})^3 + 3(w_1 - \bar{w})\sigma_1^2 \right] \\ &+ (1-a) \left[(w_2 - \bar{w})^3 + 3(w_2 - \bar{w})\sigma_2^2 \right]. \end{aligned} \quad (6)$$

Assuming the host model is able to predict the first three moments of vertical velocity, an additional two relations are required to specify the five parameters of the PDF. A number of closures have been suggested in the literature. Here, we examine some of the most recently proposed closures and compare them with the unparameterized double-Gaussian ‘‘best fit’’ PDF from the LES data. The required input moments for the closures are obtained directly from LES. This approach enables a fair comparison between the model closures, and the results reflect the best-case scenario.

The unparameterized double-Gaussian PDF parameters are determined from the LES data using an expectation maximization (EM) algorithm (Dempster et al. 1977). It is an iterative method that finds the maximum likelihood estimates of the PDF parameters, that is, the set of parameters most likely to have generated the given data. It has previously been used by Perraud et al. (2011) and Firl and Randall (2015) to determine double-Gaussian PDF parameters for clouds. Here, the EM algorithm that is part of the mixtools package in R is used (Benaglia et al. 2009) to determine the best-fit PDF parameters. It is applied at each model level in the LES over the time period specified in section 2 for each case. The results shown are averaged over the same time period.

Figure 4 shows an example of the best-fit double-Gaussian PDF determined using the EM algorithm within a stratocumulus cloud layer (DYCOMS RF01 case) and a shallow cumulus cloud layer (BOMEX case). For the stratocumulus case, Gaussian 1 represents the bulk of the cloudy points. Gaussian 2 supplements Gaussian 1 where the skewness or kurtosis departs from Gaussian. For the shallow cumulus case, Gaussian 1 instead represents the bulk of the noncloudy points. Gaussian 2 represents the tails of the distribution, including the long updraft tail representing the bulk of the cloudy points. Note that this contrasts with previous studies (e.g., Barentsen and Berkowicz 1984; Luhar et al. 1996), where Gaussian 2 is assumed to represent primarily the updraft tail only. Figure 4 also highlights that while a single-Gaussian PDF provides a good approximation for stratocumulus, it does not for shallow cumulus.

The following relations for the standard deviations of Gaussians 1 and 2 are found to provide a good fit to the LES data (Fig. 5):

$$\frac{\sigma_1}{\sigma_w} = 1 - \frac{0.4|S|}{\sqrt{0.3 + S^2}} \quad (7)$$

and

$$\frac{\sigma_2}{\sigma_w} = \begin{cases} 1, & \text{if } |K - 3| < 0.5 \\ 1.26|K - 3|^{0.28}, & \text{if } |K - 3| \geq 0.5, \end{cases} \quad (8)$$

where S and K are the skewness and kurtosis of vertical velocity, respectively, provided by the host model. The latter may be provided by the host model or diagnosed using Eq. (2) or (3). Equation (7) ensures that as $S \rightarrow 0$, $\sigma_1 \rightarrow \sigma_w$. In addition, from Eq. (8), when K is close to Gaussian, $\sigma_2 = \sigma_w$. As a result, the PDF collapses to a single Gaussian under these conditions. When K departs from Gaussian, σ_2 scales with K [Eq. (8)]. From Fig. 4b it is intuitive that this should be the case, as Gaussian 2

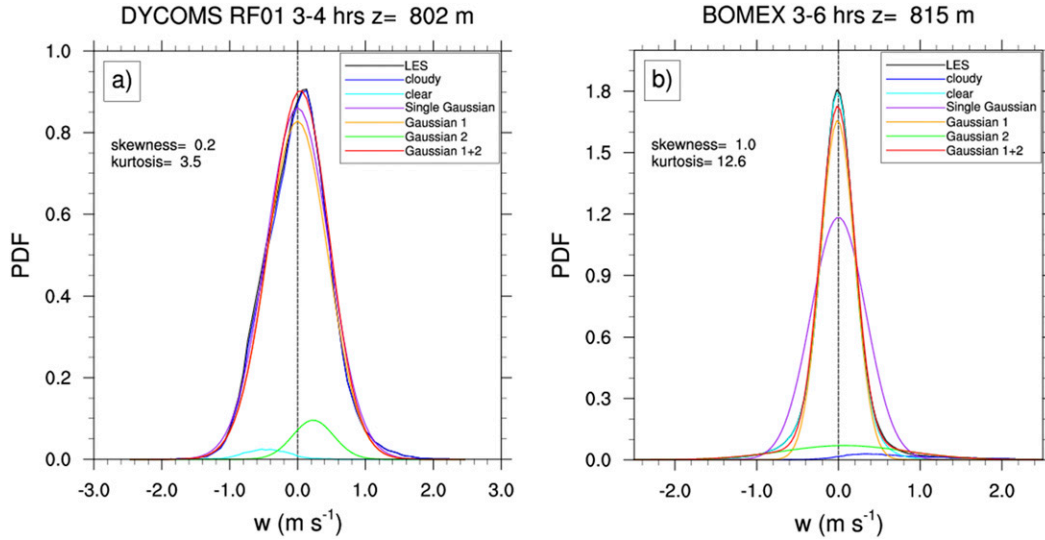


FIG. 4. The vertical velocity PDF within the cloud layer for (a) DYCOMS RF01 and (b) BOMEX. Black shows results from LES, with cloudy points shown in dark blue, and clear points shown in light blue. Purple shows the single-Gaussian PDF with a standard deviation equal to the LES. Red shows the double Gaussian best fit, which is the sum of Gaussian 1 (orange), and Gaussian 2 (green).

represents the tails of the PDF for cases with high kurtosis. Once σ_1 and σ_2 are obtained, the remaining three PDF parameters may be found by solving the first three double-Gaussian moment equations [Eqs. (4)–(6)].

Figure 5 shows vertical mean profiles of σ_1 and σ_2 for each case, where “New” denotes the new closure with kurtosis provided by the LES (or the host model), “New diag” with kurtosis instead diagnosed using Eq. (2), and “New diag S” with kurtosis diagnosed using Eq. (3). The most recent closures proposed in the literature are compared: The first one is the closure from LY. The second one is the closure from Luhar et al. (1996), with a sign modification by Larson et al. (2002) to permit both negative and positive S and called analytic double Gaussian 2 (L96/ADG2). The latter is also the closure used by Cheng and Xu (2006, 2008, 2015) in their model called Intermediately Prognostic Higher-Order Turbulence Closure (IPHOC). Finally, we compare the closure from Larson and Golaz (2005), used in their model called Cloud Layers Unified by Binormals (CLUBB), and denoted here by the same name.

For the marine shallow cumulus cases, BOMEX and RICO, the new closure for σ_1 provides a good fit to the LES data over the whole vertical profile. It performs similarly to the other closures in the subcloud layer. Differences appear in the cloud layer, with L96/ADG2 and, to a lesser degree, LY underestimating σ_1 in the middle of the cloud layer. CLUBB also underestimates σ_1 in the upper half of the cloud and above. However, these differences are not great compared to those of σ_2 . In the lower half of the subcloud layer, all the closures

apart from CLUBB perform similarly for σ_2 and provide a reasonable fit to the LES data. However, in the upper half of the subcloud layer and the lowermost levels of the cloud, the new diagnostic closure and LY and L96/ADG2 somewhat underestimate σ_2 . The new closure with predicted kurtosis provides a better fit to LES. At higher levels in the cloud, the closures deviate further, with LY, L96/ADG2, and CLUBB all substantially underestimating σ_2 . The new prognostic closure provides a much better fit to LES, with the new diagnostic closure also providing a reasonable fit with some underestimation in the lower and upper levels of the cloud. CLUBB assumes $\sigma_2 = \sigma_1$, which from Fig. 5 is not a reasonable assumption, particularly in the cloud layer.

For the continental shallow cumulus case, ARM, the models generally overestimate σ_1 somewhat in the subcloud layer, more so than in the marine shallow cumulus cases. CLUBB provides the best estimate of σ_1 in the subcloud layer, and the new closure performs similarly to the other models. These differences diminish in the cloud layer and above. For σ_2 , the new closure, LY, and L96/ADG2 perform similarly in the lower half of the subcloud layer and then diverge above, with the new closure somewhat overestimating σ_2 . Again, the greatest differences are seen in the cloud layer, with LY, L96/ADG2, and CLUBB all underestimating σ_2 significantly. The new diagnostic closure performs better, although it still underestimates σ_2 with respect to the new prognostic closure. The latter somewhat overestimates σ_2 in the cloud layer, although it provides the best fit to

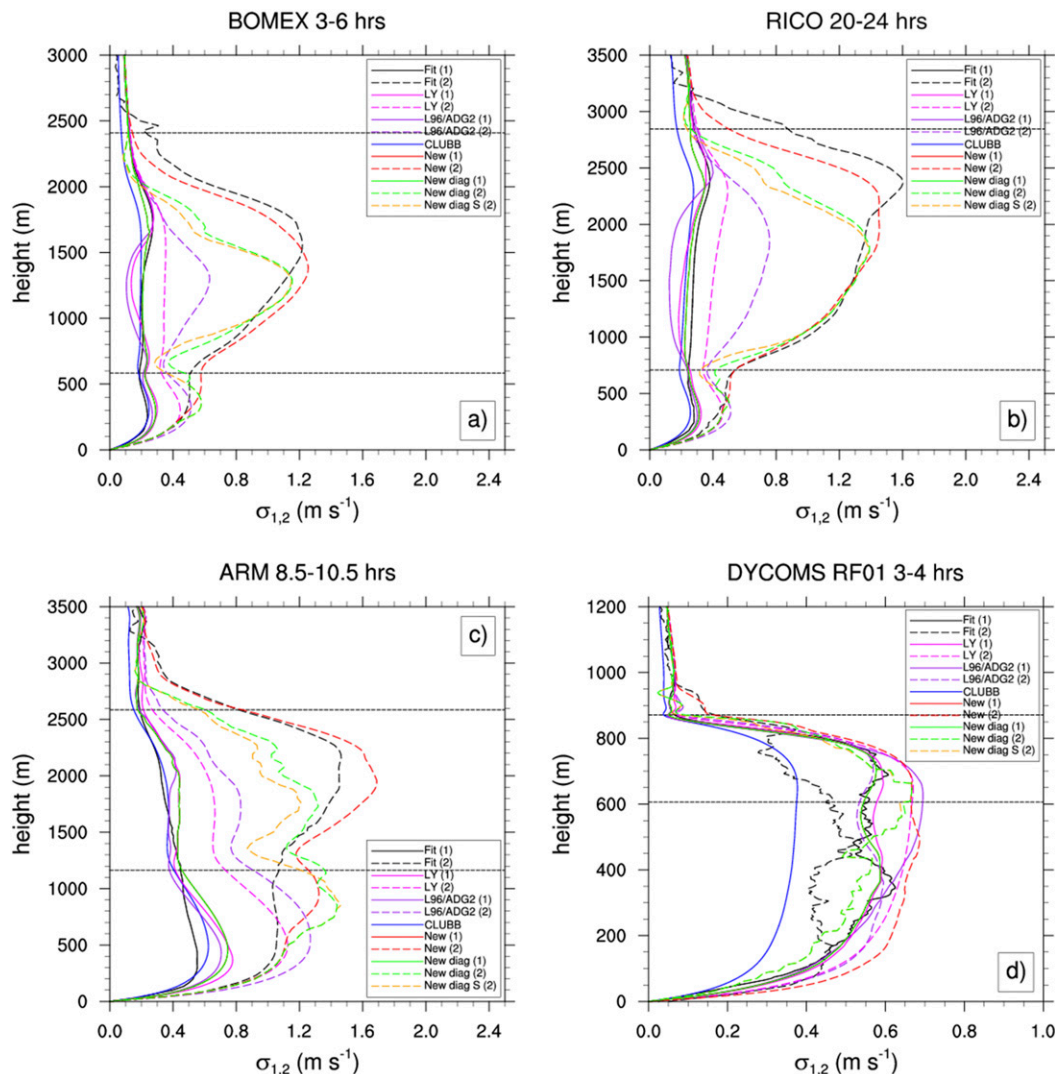


FIG. 5. Vertical mean profiles of the standard deviation of Gaussian 1 and 2 for (a) BOMEX, (b) RICO, (c) ARM, and (d) DYCOMS RF01. Black shows the double Gaussian best fit, and the closures of LY, L96/ADG2, and CLUBB are shown in magenta, purple, and blue, respectively. Note for CLUBB, $\sigma_2 = \sigma_1$. Results with the new prognostic and diagnostic closure are shown in red and green, respectively. The orange dashed line shows σ_2 obtained using K diagnosed from Eq. (3). Horizontal dashed lines indicate the cloud layer.

the LES over the vertical column with respect to the other models.

Finally, for the stratocumulus case, DYCOMS RF01, the new closure and LY provide a good fit to the LES for σ_1 . L96/ADG2 somewhat overestimates σ_1 in the upper half of the subcloud layer and the lower half of the cloud layer. CLUBB underestimates σ_1 in the subcloud and cloud layers by approximately one-third. For σ_2 , the new closure, LY, and L96/ADG2 generally overestimate σ_2 . CLUBB underestimates σ_2 , apart from in the cloud layer, where it provides a better fit. However, it should be noted that the differences with respect to the best fit

for this case are much smaller for all the models than for the shallow cumulus cases.

6. Cloud-layer vertical velocity PDFs

Here we examine the vertical velocity PDF within the cloud layer for the different cases, comparing the LES PDF with the various double-Gaussian closures. Figures 6 and 7 show the vertical velocity PDF for each case at a level in the cloud where skewness is around maximum, to highlight differences in the double-Gaussian closures. The right-hand column has a log scale to highlight differences in the tails.

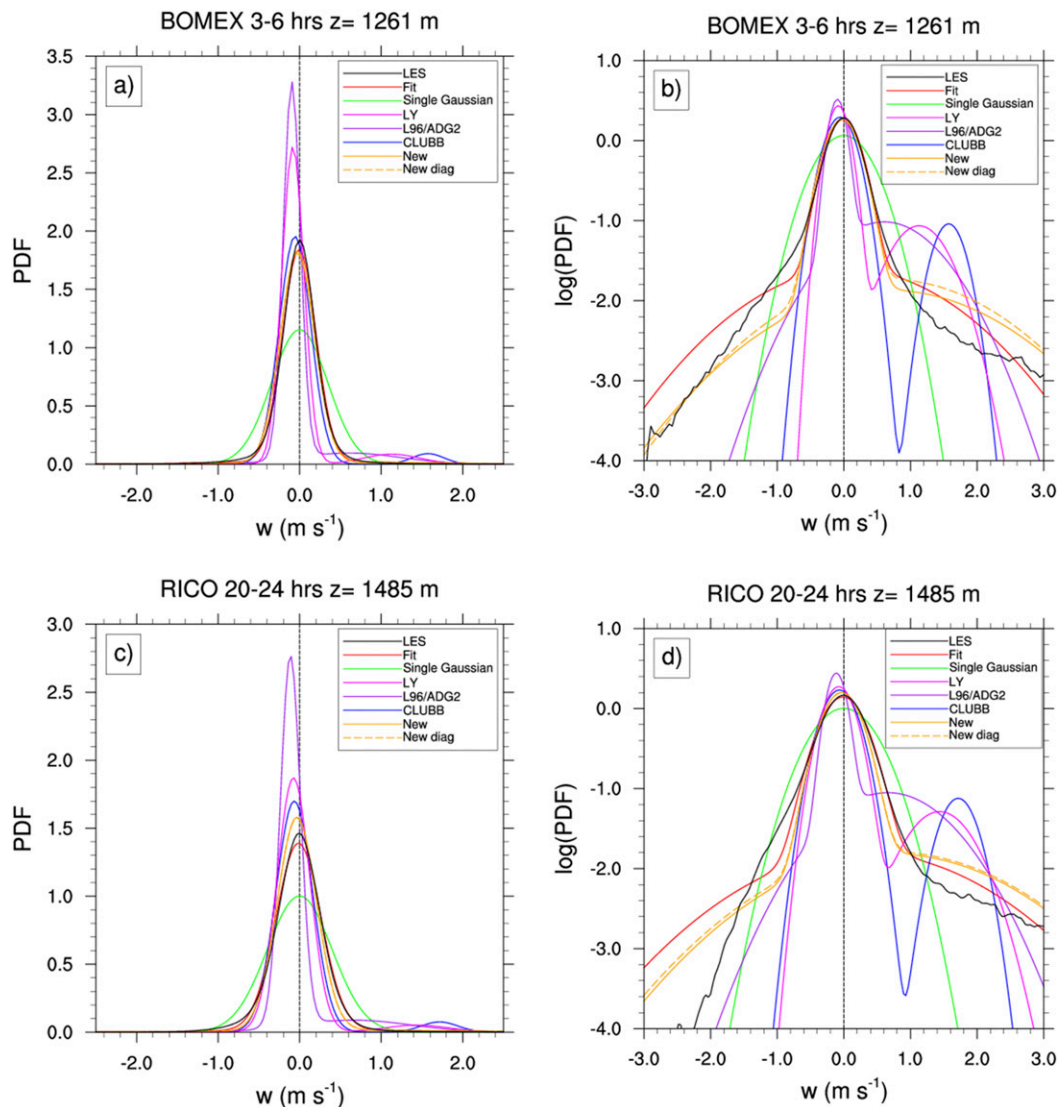


FIG. 6. The vertical velocity PDF within the cloud layer for (a),(b) BOMEX and (c),(d) RICO. The PDF with a log scale is shown in (b) and (d). The PDF from LES is shown in black, and the double- and single-Gaussian best fits are shown in red and green, respectively. The closures from LY, L96/ADG2, and CLUBB are shown in magenta, purple, and blue, respectively. Results with the new prognostic and diagnostic closure are shown in solid and dashed orange, respectively.

The shallow cumulus cases are characterized by strongly non-Gaussian turbulence statistics, with PDFs displaying high skewness and kurtosis. The amplitude of Gaussian 1 is significantly overestimated by LY and L96/ADG2 for BOMEX (Figs. 6a,b), whereas CLUBB and the new closure provide a good estimate of the amplitude. As discussed in the previous section, LY and L96/ADG2 underestimate σ_1 , which is also seen in Fig. 6. For the updraft tail, representing the bulk of the cloudy points, LY and L96/ADG2 overestimate the probability of w values between approximately 0.4 and 2.3 m s^{-1} . Above this value, the probability is underestimated

owing to a smaller σ_2 , which results in a more rapid decay of the PDF. CLUBB displays the greatest bimodality of all the PDFs, because $\sigma_2 = \sigma_1$ and there is greater separation between w_1 and w_2 . As a result, it tends to underestimate the probability of w at intermediate values (here, between around 0.5 and 1.2 m s^{-1}) and overestimate the probability at higher values (here, between 1.2 and 2.2 m s^{-1}). There is an underestimation at higher values, as with LY and L96/ADG2, owing to a smaller σ_2 , which results in a more rapid decay of the PDF. These models also significantly underestimate the downdraft tail of the PDF, by a factor of 100 in some cases.

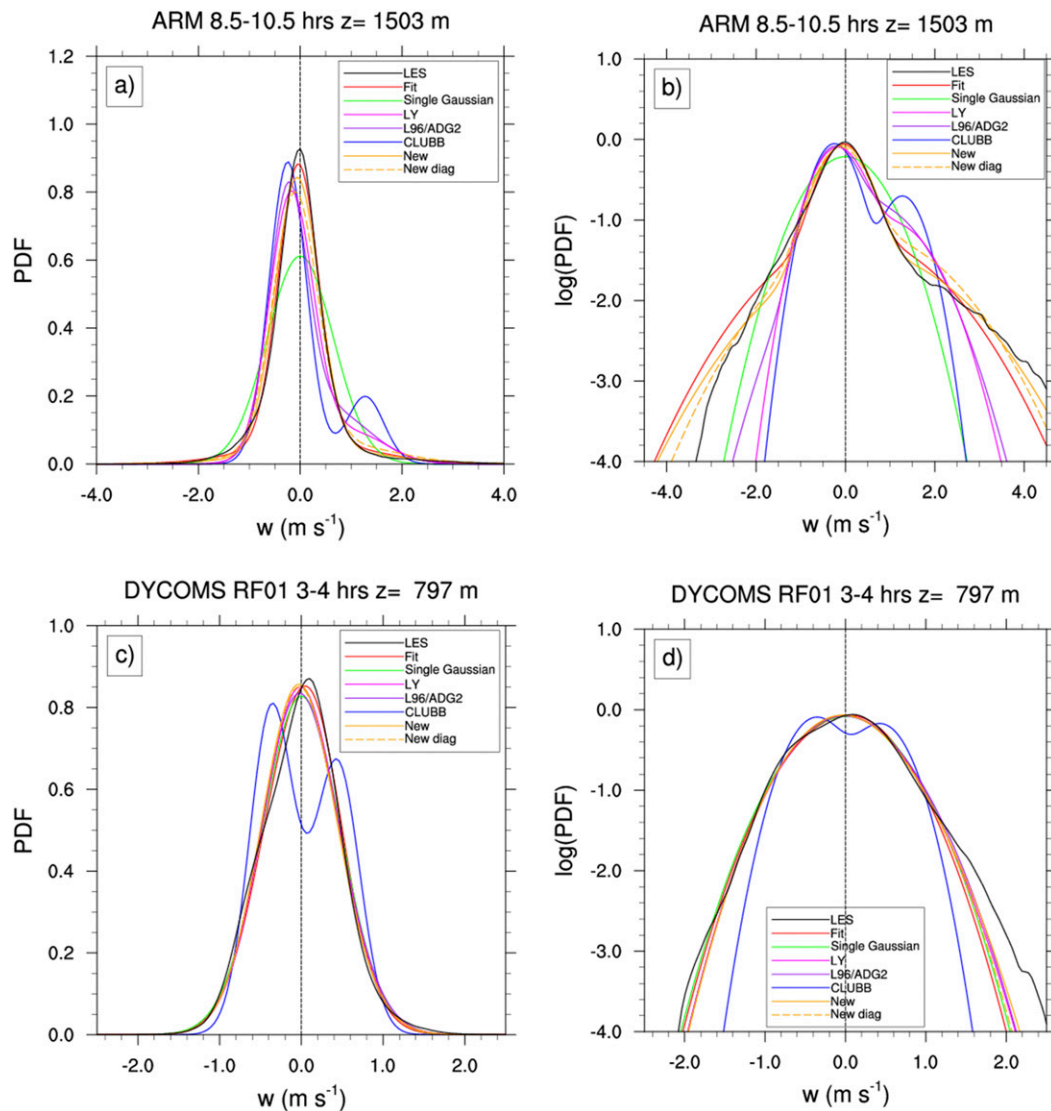


FIG. 7. As in Fig. 6, but for (a),(b) ARM and (c),(d) DYCOMS RF01.

The new closure performs well compared to LES, with the tails of the PDF decaying less rapidly owing to larger σ_2 . The errors are within an order of magnitude.

Similar differences between the models are seen for RICO, although there is less overestimation of the amplitude of Gaussian 1 for LY (Figs. 6c,d). CLUBB and, to a lesser degree, the new closure somewhat overestimate the amplitude. The updraft tail is a little longer and fatter than the BOMEX case, and all the models capture this. The new closure performs well for the updraft tail. It overestimates the downdraft tail for this case, although it should be noted that the double-Gaussian best fit also overestimates the downdraft tail, pointing to some fundamental limitations of the double-Gaussian formulation.

The ARM case is driven by stronger surface fluxes over land, relative to the BOMEX and RICO cases. The PDF has a greater variance and longer tails as a result (Figs. 7a,b). All the models estimate the amplitude of Gaussian 1 reasonably well. However, as with BOMEX and RICO, the length of the tails is underestimated for LY, L96/ADG2, and CLUBB. The new closure performs well, both for Gaussian 1 and for the tails. The minor mode seen in CLUBB is more prominent in this case than in BOMEX and RICO, and results in an overestimation of the probability of w values between 0.8 and 2 m s^{-1} .

Finally, for DYCOMS RF01, LY, L96/ADG2, and the new closure perform well, with minimal differences seen (Figs. 7c,d). The single Gaussian also provides a good

estimate of the PDF. However, CLUBB exhibits a bimodal PDF, with the antimode occurring at the modal value of the LES PDF. The formulation of CLUBB does not allow it to collapse to a single Gaussian for low skewness as with the other closures. It also underestimates the probability in the tails.

7. Updraft probability

The integral of the w PDF over a particular interval is the probability of w values occurring within that interval. For cloud and aerosol physics, we are particularly interested in the updraft portion of the PDF, where cloud forms. Here, we examine the PDF integrals for positive w , which provides an overall measure of the quality of the PDF.

The shallow cumulus cases show similar updraft probability characteristics overall from the LES (Fig. 8). In the subcloud layer, the probability of an updraft lies between 0.4 and 0.5. This probability is equivalent to the updraft fractional area over the domain, an important component of mass-flux cumulus models. The probability decreases with height from the surface and reaches a minimum in the mid- to upper half of the subcloud layer. From this point it increases again until inside the cloud layer, where the probability lies around 0.5. For the marine shallow cumulus cases (BOMEX and RICO), the updraft probability is slightly less than 0.5 for much of the cloud layer. It increases slightly above 0.5 in the upper cloud layer, before becoming approximately constant around 0.5 above. The continental shallow cumulus case (ARM) shows a greater variation in updraft probability in the cloud layer as a result of stronger fluxes.

The stratocumulus case (DYCOMS RF01) displays opposite updraft probability characteristics to the shallow cumulus cases. For this case, the updraft probability gradually increases with height within the subcloud layer, from about 0.48 near the surface to 0.54 at the base of the cloud. The probability increases above 0.5 around the midpoint of the subcloud layer. The probability stays roughly constant in the lower half of the cloud layer, at around 0.54, and then decreases with height to the top of the cloud layer, where it reaches a minimum of 0.45. This minimum is a reflection of the cloud-top radiative cooling driving negative buoyancy. Above the cloud layer, the updraft probability increases again to around 0.5.

The greatest differences between the models are seen for the BOMEX and RICO cases. LY, L96/ADG2, and the new closure slightly overestimate the updraft probability from the surface to the upper subcloud layer. Above this height agreement is better, although the results diverge again around the cloud base, where the new closure (with predicted kurtosis) performs the best. CLUBB

underestimates the updraft probability throughout the subcloud layer, by up to 10% for RICO. Going into the cloud layer, the models diverge further, with all underestimating the probability through much of the cloud layer. L96/ADG2 underestimates the probability the most, by up to 45% in both cases. LY underestimates the probability to a lesser degree, by up to 35% in BOMEX and 25% in RICO. CLUBB performs similarly for BOMEX and RICO, underestimating the probability by up to 20%. The new prognostic closure performs best, underestimating the updraft probability by up to 6%. Around cloud top and above, the models perform similarly to the LES, although L96/ADG2 and CLUBB slightly overpredict the updraft probability near the top of the cloud for RICO.

The models show somewhat similar characteristics for ARM as BOMEX and RICO within the subcloud layer. However, model performance is generally improved overall for the cloud layer. Here, the updraft probability is underestimated by up to 20%, 17%, 14%, and 4% for L96/ADG2, CLUBB, LY, and the new prognostic closure, respectively. Above the cloud layer, LY and the new closure perform best, with results similar to LES. CLUBB and L96/ADG2 underestimate the probability by up to 10%.

Of all the cases, the models perform best for DYCOMS RF01, with less variation between them. The better agreement results from the low skewness for this case. CLUBB shows the greatest deviation from the LES, with the updraft probability overestimated by up to 6% near cloud base and underestimated by up to 16% near cloud top. LY, L96/ADG2, and the new closure deviate from LES from the upper subcloud layer to the upper half of the cloud layer, with the updraft probability underestimated by up to 6%. No model performs best for cloud base, with LY, L96/ADG2, and the new closure underestimating, and CLUBB overestimating the probability, by approximately the same degree. At cloud top, the new prognostic closure performs best, closely matching LES. Above the cloud layer, the models perform similarly to LES, with greater deviations seen in CLUBB.

For the strongest updrafts, where $w > 2\sigma_w$, most of the models significantly overestimate the probability within the cloud layer for the shallow cumulus cases (Fig. 9). The new closure greatly reduces this overestimation, with the probability overestimated by up to 20% and 56% for the prognostic and diagnostic closures, respectively, for BOMEX. LY, L96/ADG2, and CLUBB overestimate the probability by up to a factor of 4.4, 4.1, and 3.4, respectively. In the upper cloud layer and above, CLUBB underestimates the probability by up to 60%. A similar pattern is seen for RICO.

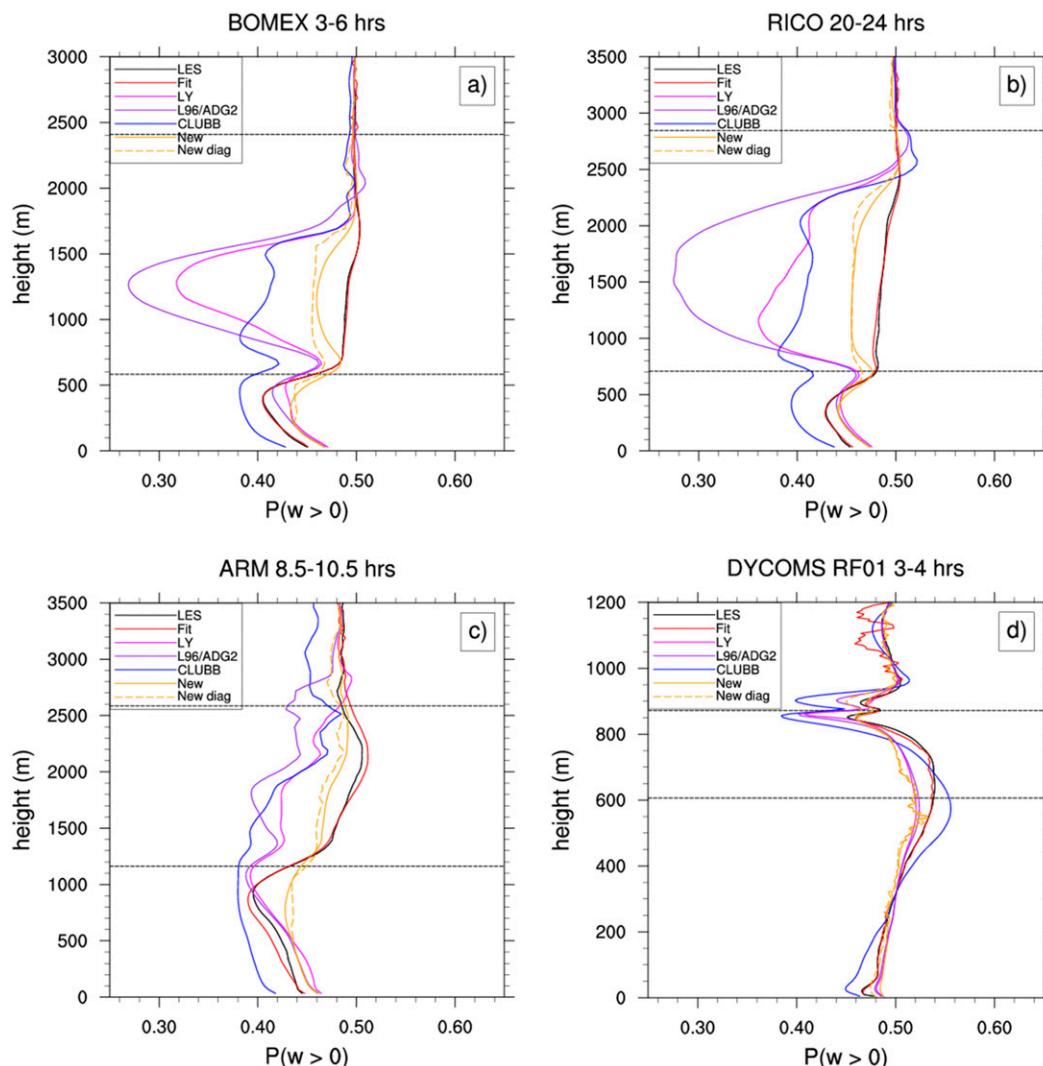


FIG. 8. Vertical mean profiles of the updraft probability ($w > 0$) for (a) BOMEX, (b) RICO, (c) ARM, and (d) DYCOMS RF01. Curves are as in Fig. 7. Horizontal dashed lines indicate the cloud layer.

For ARM, the overestimation of the probability is generally reduced compared to BOMEX and RICO. The probability is overestimated up to a factor of 2.4, 2.2, and 2.2, for CLUBB, LY, and L96/ADG2, respectively, within the cloud layer. The overestimation is significantly reduced for the new closure, with the probability overestimated by up to 20% and 47% for the prognostic and diagnostic closures, respectively. Overall, the new prognostic closure provides the best estimate of the probability of strong updrafts, and it most closely follows the shape of the LES profile.

As before, the models show better agreement for DYCOMS RF01. LY, L96/ADG2, and the new closure all provide a reasonable estimate of the probability within most of the cloud layer. However, the models diverge near the cloud top, with the new closure in

good agreement with LES, and CLUBB, LY, and L96/ADG2 overestimating the probability by up to 70%, 50%, and 42%, respectively. Apart from around cloud top, CLUBB significantly underestimates the probability relative to LES and the other models by around 60%.

8. Closure of higher-order moments

Once the double-Gaussian PDF has been specified, it may be used to diagnose higher-order moments, such as w^4 . These higher-order moments may then be used to close the predictive equations for lower-order moments at the next model time step. The higher-order moments may be diagnosed from the PDF by integrating the moment over the PDF. The resulting equation for w^4 is

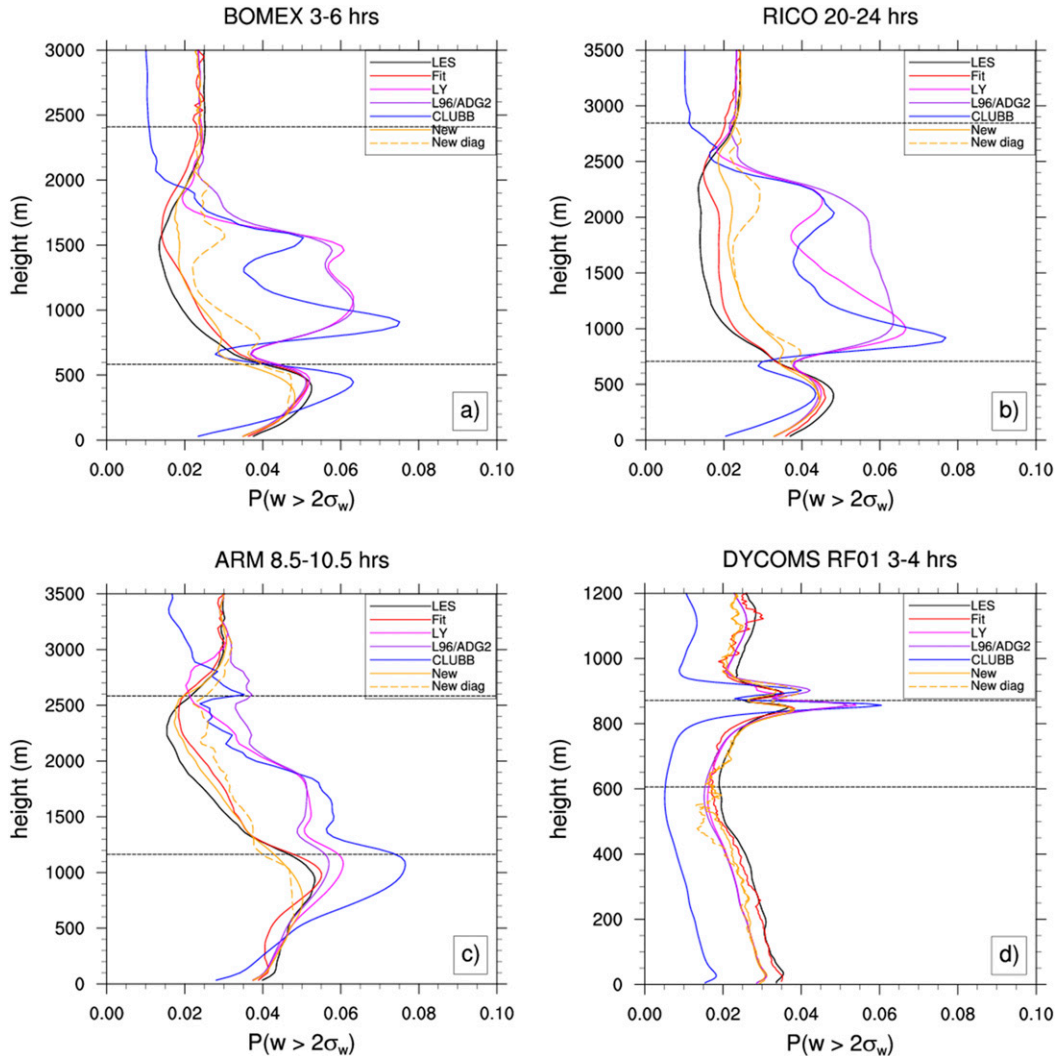


FIG. 9. Vertical mean profiles of the updraft probability for $w > 2\sigma_w$ for (a) BOMEX, (b) RICO, (c) ARM, and (d) DYCOMS RF01. Curves are as in Fig. 7. Horizontal dashed lines indicate the cloud layer.

$$\overline{w^4} = a \left[(w_1 - \bar{w})^4 + 6(w_1 - \bar{w})\sigma_1^2 + 3\sigma_1^4 \right] + (1 - a) \left[(w_2 - \bar{w})^4 + 6(w_2 - \bar{w})\sigma_2^2 + 3\sigma_2^4 \right]. \quad (9)$$

Figure 10 shows $\overline{w^4}$ resulting from the different model closures, compared with LES. For the shallow cumulus cases, the new closure significantly improves performance within the cloud layer. LY, L96/ADG2, and CLUBB show similar results, underestimating the peak in $\overline{w^4}$ by 69%, 67%, and 63% for the BOMEX, RICO, and ARM cases, respectively. While results are improved with the new closure, the peak is still underestimated by 34%, 28%, and 22% for the BOMEX, RICO, and ARM cases, respectively, for the prognostic closure. The peak is underestimated by

38%, 37%, and 29%, for the BOMEX, RICO, and ARM cases, respectively, for the diagnostic closure. Note that the double-Gaussian best fit does not improve performance, indicating a fundamental limitation with the double-Gaussian PDF. In this case, increasing the number of Gaussians to 3 or 4 would be necessary to improve the results (Firl and Randall 2015).

In the subcloud layer, the model results converge, with the new prognostic closure, LY, and L96/ADG2 performing slightly better than CLUBB for BOMEX and RICO. The new prognostic closure performs best in the upper subcloud layer and around cloud base. For the ARM case, LY, L96/ADG2, and the new closure somewhat overestimate the peak in $\overline{w^4}$ in the subcloud layer by around 20%. CLUBB performs better in this case.

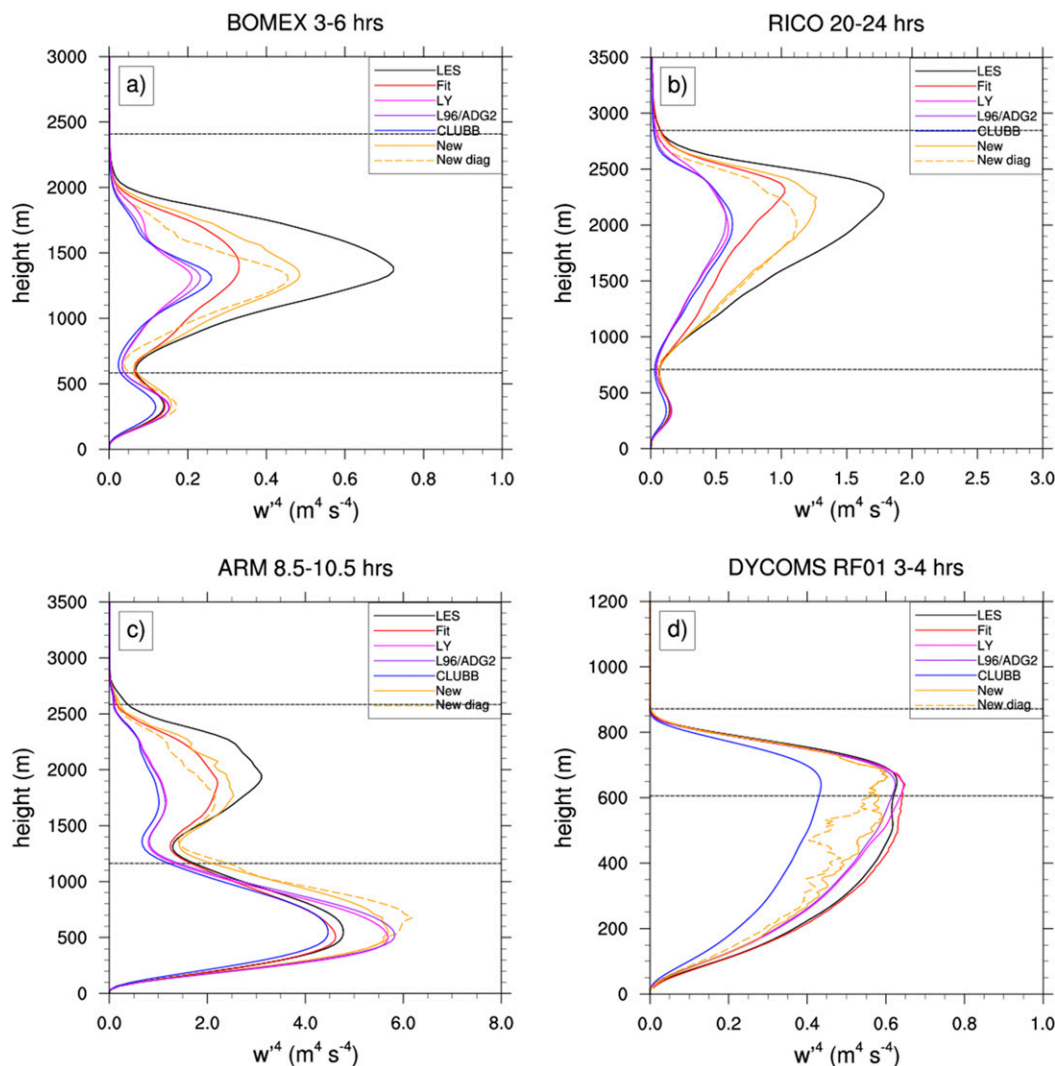


FIG. 10. Vertical mean profiles of the fourth moment of w for (a) BOMEX, (b) RICO, (c) ARM, and (d) DYCOMS RF01. Curves are as in Fig. 7. Horizontal dashed lines indicate the cloud layer.

For DYCOMS RF01, the new closure, LY, and L96/ADG2 perform similarly within the cloud layer, giving good agreement with LES. However, CLUBB underestimates the peak by 30%. In the subcloud layer, the new prognostic closure, LY, and L96/ADG2 perform slightly worse than in the cloud layer. The new diagnostic closure underestimates w^4 by up to 32% in the upper subcloud layer but performs similarly to the prognostic closure otherwise. CLUBB consistently underestimates w^4 by 30%–38% within the subcloud layer.

9. Discussion and conclusions

We have examined the vertical velocity probability distribution function (PDF) throughout the depth of the lower atmosphere, including the cloud layer and above,

in large-eddy simulations (LESs) of four GASS boundary layer cloud intercomparison cases. To our knowledge, this is the first study to do so. Two marine shallow cumulus cases (BOMEX and RICO), a continental shallow cumulus case (ARM), and a marine stratocumulus case (DYCOMS RF01) are studied. DYCOMS RF01 exhibits largely Gaussian vertical velocity statistics, typical of stratocumulus cloud, and, in this case, representing the vertical velocity PDF with a single Gaussian will suffice. However, the shallow cumulus cases are characterized by non-Gaussian turbulence statistics with large departures from Gaussian values for higher-order moments such as skewness and kurtosis in the cloud layer. For these cases, a PDF that is able to represent such non-Gaussian turbulence statistics is required. A double-Gaussian PDF is one of the simplest

distributions that will permit non-Gaussian values of higher-order moments, and it has been employed to represent turbulence by LY, Luhar et al. (1996), Larson et al. (2002), and Larson and Golaz (2005) among others. These model closures for the vertical velocity PDF have been examined, with the required input statistical moments obtained directly from LES. This approach enables a fair comparison between the model closures, and the results reflect the best-case scenario. We do not examine the impact of inaccuracies in the various “host” models (i.e., the higher-order turbulence models used to predict the required moments to construct the double-Gaussian PDF in an atmospheric model). Neither do we test the applicability of the model closures across a range of model grid sizes. Bogenschutz et al. (2010) found little sensitivity to grid size for double-Gaussian PDFs applied to shallow cumulus.

Existing model PDF closures are found to perform well overall in the subcloud layer for the shallow cumulus cases. However, they break down in the cloud layer, where vertical velocity statistics become strongly non-Gaussian and high skewness and kurtosis are seen. Inaccuracies are seen in both the amplitude and standard deviation of the first Gaussian, representing primarily clear air, and the second Gaussian, representing the tails. The latter includes the updraft tail, consisting mostly of cloudy air. The tails of the PDF decay too rapidly, underestimating extreme values. At intermediate values within the updraft tail, the probability tends to be overestimated. For updrafts greater than $2\sigma_w$, existing closures overestimate the probability by a factor of 3–4 for BOMEX and RICO, and by more than a factor of 2 for ARM. However, the probability of updrafts overall (i.e., the probability of any value of vertical velocity greater than zero) is underestimated by existing closures, by 20%–45% for BOMEX and RICO. For ARM, the underestimation is reduced to 14%–20%. As a result, convective transport would be underestimated in these models. In addition, the number of activated aerosol particles within cumulus clouds would be underpredicted, leading to a bias in the first AIE.

For the stratocumulus case, the majority of the models perform well overall, in both the subcloud and cloud layer. There is also much better agreement between the models, with the exception of CLUBB. The latter produces a bimodal PDF, owing to its formulation, which does not collapse to a single Gaussian with low skewness. However, it still produces a reasonable overall probability of updrafts, apart from updrafts greater than $2\sigma_w$, where the probability is underestimated by around 60% throughout most of the subcloud and cloud layers.

To diagnose the source of bias in existing model closures and to guide development of an improved closure, an unparameterized double-Gaussian best fit to the LES

was obtained using an expectation maximization (EM) algorithm. This analysis highlighted shortcomings in specifying the standard deviation of the second Gaussian σ_2 representing the tails of the PDF. While existing closures perform well overall in the subcloud layer and above the cloud layer, where higher-order moments are relatively small, they are found to significantly underestimate σ_2 in shallow cumulus cloud layers. Here, there are significant departures from Gaussian values in the skewness and kurtosis. The underestimation of σ_2 is the main reason behind the bias in the updraft tail of the PDF discussed above. It is intuitive that as the kurtosis increases—that is, the probability of extreme values increases— σ_2 should also increase. An empirical power-law relationship between σ_2 and the kurtosis was found that gives a much better estimation of σ_2 within shallow cumulus cloud layers. It should be noted that one of the model closures examined, L96/ADG2, was not designed to be applied in cloudy boundary layers. Rather, it was originally developed for use in Lagrangian stochastic dispersion models in the subcloud layer. Another of the model closures examined, CLUBB, assumes equal standard deviations of the two Gaussians, that is, $\sigma_2 = \sigma_1$. The unparameterized double-Gaussian fit showed this to be a poor assumption, in agreement with Firl and Randall (2015). For the stratocumulus case, the model closures performed well over the entire vertical column, with the exception of CLUBB, which underestimates $\sigma_{1,2}$ by around one-third in both the subcloud and cloud layers. Guo et al. (2015) found $\sigma_{1,2}$ in CLUBB to be a key control on the global mean low-cloud fraction and shortwave cloud forcing, especially in subtropical regions dominated by stratus.

The new closure relies on knowledge of the vertical velocity kurtosis, or the fourth moment of vertical velocity. If the host model is able to predict the fourth moment, then it may be immediately used to specify the double-Gaussian PDF. The best results are obtained with this method. However, most higher-order turbulence models predict only the third moment at most. In this case, the kurtosis must be diagnosed from lower-order moments. A parabolic relationship between skewness and kurtosis has been found for this purpose (Mole and Clarke 1995; GH; Waggy et al. 2016). These relationships are in good agreement with the LES results within the subcloud layer. However, they break down in the cloud layer, where the kurtosis increases more rapidly with skewness than in these relations. The parabolic relationship is modified here for use in the cloud layer, which provides a much better estimate of the kurtosis. To our knowledge, this relationship has not been previously examined beyond the subcloud layer. The different behavior within the cloud layer is due to enhanced turbulence

from latent heat release. The new parabolic relationship is split into two regimes, one for the cloud layer and one outside the cloud layer. If no information is available regarding the cloud layer, then the appropriate regime may also be identified based on only the skewness, with lower values of skewness assumed outside the cloud layer. The resulting relationship appears to perform well for the cases studied here; however, it is recommended more cases be studied in future. A preliminary analysis of the LES ARM Symbiotic Simulation and Observation (LASSO) dataset (Gustafson et al. 2017) has also revealed the different nature of the parabolic relationship in cumulus cloud layers. Model studies of vertical velocity kurtosis within shallow cumulus layers are scarce, although the few available are qualitatively in agreement with the current work. In addition, observations of vertical velocity skewness and kurtosis within cloud layers are particularly in short supply to verify the results seen here.

Estimation of the vertical velocity PDF is much improved with the new closure for the shallow cumulus cases, for both the mode and the tails. The overall updraft probability is also in much better agreement with LES, with the probability underestimated by no more than 10%. In addition, the probability of updrafts greater than $2\sigma_w$, representing mostly cloudy points, shows much improvement, with overestimation reduced by a factor of 2–4.

Once the double-Gaussian PDF is specified, it may be used to diagnose higher-order moments, such as w^4 . These moments may then be used to close the predictive equations for lower-order moments at the next model time step. The third- and fourth-order moments, in particular, are key controls in the convective heat transport in the CBL (e.g., Waggy et al. (2016)). An improved formulation of w^4 was found to be more important by Cheng and Xu (2006) for diagnosing the cloud fraction than the turbulence-scale condensation scheme. The new closure greatly improves the underestimation of w^4 within cumulus cloud layers, by around one-half. However, w^4 is still underestimated, although it should be noted that its performance is similar to the unparameterized double-Gaussian PDF. The latter points to some fundamental limitations, with the double-Gaussian PDF unable to represent extreme departures from Gaussian turbulence statistics, seen in the center of cumulus cloud layers examined here. In this regime, additional Gaussians would be required to represent the updraft and downdraft tails individually, as well as the mode. This issue is highlighted in the PDF results, with the unparameterized PDF unable to represent both tails equally well, and with some underestimation in the amplitude of the mode. Firl and Randall (2015) found that four Gaussians are necessary to represent w^3 in

cumulus cloud layers, while only two are needed in the subcloud layer and for stratocumulus, suggesting that this points to the different nature of turbulence statistics within cumulus cloud layers. Here, the results confirm that the turbulence statistics are very different in cumulus cloud layers, and one of the main novel findings is that it is the very high skewness and kurtosis that separate cumulus cloud layers from other regimes, and why existing model closures perform relatively poorly there.

The main drawback with the new closure is that it requires numerically solving the moment equations to find the amplitudes and means of the Gaussians after the standard deviations have been specified. As a result, it is more computationally expensive than an analytical formulation. As with existing closures, it relies on the ability of the host model to accurately predict the higher-order moments of vertical velocity, in particular w^3 . However, it improves performance significantly for shallow cumulus cloud layers, in addition to performing well for stratocumulus. Future work will involve assessing the new closure in a host model for use in weather and climate prediction.

Acknowledgments. I would like to express my appreciation to Steven Ghan and the Atmospheric Sciences and Global Change Division at PNNL for their hospitality and support during my visit, when much of this work was carried out. I would also like to thank Grant Firl and one anonymous reviewer for their constructive comments. Partial funding is gratefully acknowledged from the EU APPLICATE Project 727862, and the Climate Model Development and Validation program funded by the Office of Biological and Environmental Research in the U.S. Department of Energy (DOE) Office of Science. The Pacific Northwest National Laboratory (PNNL) is operated for the DOE by Battelle Memorial Institute under Contract DE-AC06-76RLO 1830. Additional funding is acknowledged from the Bolin Centre for Climate Research. Supercomputing facilities were provided by PNNL and NCAR.

REFERENCES

- Alberghi, S., A. Maurizi, and F. Tampieri, 2002: Relationship between the vertical velocity skewness and kurtosis observed during sea-breeze convection. *J. Appl. Meteor.*, **41**, 885–889, [https://doi.org/10.1175/1520-0450\(2002\)041<0885:RBTVVS>2.0.CO;2](https://doi.org/10.1175/1520-0450(2002)041<0885:RBTVVS>2.0.CO;2).
- André, J. C., G. D. Moor, P. Lacarrère, and R. D. Vachet, 1976: Turbulence approximation for inhomogeneous flows: Part I. The clipping approximation. *J. Atmos. Sci.*, **33**, 476–481, [https://doi.org/10.1175/1520-0469\(1976\)033<0476:TAFIFP>2.0.CO;2](https://doi.org/10.1175/1520-0469(1976)033<0476:TAFIFP>2.0.CO;2).
- Ansmann, A., J. Fruntke, and R. Engelmann, 2010: Updraft and downdraft characterization with Doppler lidar: Cloud-free versus cumuli-topped mixed layer. *Atmos. Chem. Phys.*, **10**, 7845–7858, <https://doi.org/10.5194/acp-10-7845-2010>.

- Bærentsen, J. H., and R. Berkowicz, 1984: Monte Carlo simulation of plume dispersion in the convective boundary layer. *Atmos. Environ.*, **18**, 701–712, [https://doi.org/10.1016/0004-6981\(84\)90256-7](https://doi.org/10.1016/0004-6981(84)90256-7).
- Benaglia, T., D. Chauveau, D. Hunter, and D. Young, 2009: mixtools: An R package for analyzing finite mixture models. *J. Stat. Software*, **32**, 1–29, <https://doi.org/10.18637/jss.v032.i06>.
- Berg, L. K., R. K. Newsom, and D. D. Turner, 2017: Year-long vertical velocity statistics derived from Doppler lidar data for the continental convective boundary layer. *J. Appl. Meteor. Climatol.*, **56**, 2441–2454, <https://doi.org/10.1175/JAMC-D-16-0359.1>.
- Bogenschutz, P. A., S. K. Krueger, and M. Khairoutdinov, 2010: Assumed probability density functions for shallow and deep convection. *J. Adv. Model. Earth Syst.*, **2**, 10, <https://doi.org/10.3894/JAMES.2010.2.10>.
- , A. Gettelman, H. Morrison, V. E. Larson, D. P. Schanen, N. R. Meyer, and C. Craig, 2012: Unified parameterization of the planetary boundary layer and shallow convection with a higher-order turbulence closure in the Community Atmosphere Model: Single-column experiments. *Geosci. Model Dev.*, **5**, 1407–1423, <https://doi.org/10.5194/gmd-5-1407-2012>.
- Bougeault, P., 1981: Modeling the trade-wind cumulus boundary layer. Part I: Testing the ensemble cloud relations against numerical data. *J. Atmos. Sci.*, **38**, 2414–2428, [https://doi.org/10.1175/1520-0469\(1981\)038<2414:MTWCB>2.0.CO;2](https://doi.org/10.1175/1520-0469(1981)038<2414:MTWCB>2.0.CO;2).
- Brown, A. R., and Coauthors, 2002: Large-eddy simulation of the diurnal cycle of shallow cumulus convection over land. *Quart. J. Roy. Meteor. Soc.*, **128**, 1075–1093, <https://doi.org/10.1256/003590002320373210>.
- Canuto, V. M., F. Minotti, C. Ronchi, R. M. Ypma, and O. Zeman, 1994: Second-order closure PBL model with new third-order moments: Comparison with LES data. *J. Atmos. Sci.*, **51**, 1605–1618, [https://doi.org/10.1175/1520-0469\(1994\)051<1605:SOCPMW>2.0.CO;2](https://doi.org/10.1175/1520-0469(1994)051<1605:SOCPMW>2.0.CO;2).
- , Y. Cheng, and A. Howard, 2001: New third-order moments for the convective boundary layer. *J. Atmos. Sci.*, **58**, 1169–1172, [https://doi.org/10.1175/1520-0469\(2001\)058<1169:NTOMFT>2.0.CO;2](https://doi.org/10.1175/1520-0469(2001)058<1169:NTOMFT>2.0.CO;2).
- Cheng, A., and K.-M. Xu, 2006: Simulation of shallow cumuli and their transition to deep convective clouds by cloud-resolving models with different third-order turbulence closures. *Quart. J. Roy. Meteor. Soc.*, **132**, 359–382, <https://doi.org/10.1256/qj.05.29>.
- , and —, 2008: Simulation of boundary-layer cumulus and stratocumulus clouds using a cloud-resolving model with low- and third-order turbulence closures. *J. Meteor. Soc. Japan*, **86A**, 67–86, <https://doi.org/10.2151/jmsj.86A.67>.
- , and —, 2015: Improved low-cloud simulation from the Community Atmosphere Model with an advanced third-order turbulence closure. *J. Climate*, **28**, 5737–5762, <https://doi.org/10.1175/JCLI-D-14-00776.1>.
- Ching, J., N. Riemer, M. Dunn, and M. Miller, 2010: In-cloud turbulence structure of marine stratocumulus. *Geophys. Res. Lett.*, **37**, L21808, <https://doi.org/10.1029/2010GL045033>.
- Chu, C. R., M. B. Parlange, G. G. Katul, and J. D. Albertson, 1996: Probability density functions of turbulent velocity and temperature in the atmospheric surface layer. *Water Resour. Res.*, **32**, 1681–1688, <https://doi.org/10.1029/96WR00287>.
- Cristelli, M., A. Zaccaria, and L. Pietronero, 2012: Universal relation between skewness and kurtosis in complex dynamics. *Phys. Rev.*, **85E**, 066108, <https://doi.org/10.1103/PhysRevE.85.066108>.
- Deardorff, J. W., 1980: Stratocumulus-capped mixed layers derived from a three-dimensional model. *Bound.-Layer Meteor.*, **18**, 495–527, <https://doi.org/10.1007/BF00119502>.
- Dempster, A. P., N. M. Laird, and D. B. Rubin, 1977: Maximum likelihood from incomplete data via the EM algorithm. *J. Roy. Stat. Soc.*, **39B**, 1–38.
- Donner, L. J., T. A. O'Brien, D. Rieger, B. Vogel, and W. F. Cooke, 2016: Are atmospheric updrafts a key to unlocking climate forcing and sensitivity? *Atmos. Chem. Phys.*, **16**, 12 983–12 992, <https://doi.org/10.5194/acp-16-12983-2016>.
- Du, S., J. D. Wilson, and E. Yee, 1994: Probability density functions for velocity in the convective boundary layer, and implied trajectory models. *Atmos. Environ.*, **28**, 1211–1217, [https://doi.org/10.1016/1352-2310\(94\)90298-4](https://doi.org/10.1016/1352-2310(94)90298-4).
- Firl, G. J., and D. A. Randall, 2015: Fitting and analyzing LES using multiple trivariate Gaussians. *J. Atmos. Sci.*, **72**, 1094–1116, <https://doi.org/10.1175/JAS-D-14-0192.1>.
- Ghate, V. P., B. A. Albrecht, M. A. Miller, A. Brewer, and C. W. Fairall, 2014: Turbulence and radiation in stratocumulus-topped marine boundary layers: A case study from VOCALS-REx. *J. Appl. Meteor. Climatol.*, **53**, 117–135, <https://doi.org/10.1175/JAMC-D-12-0225.1>.
- Gryanik, V. M., and J. Hartmann, 2002: A turbulence closure for the convective boundary layer based on a two-scale mass-flux approach. *J. Atmos. Sci.*, **59**, 2729–2744, [https://doi.org/10.1175/1520-0469\(2002\)059<2729:ATCFTC>2.0.CO;2](https://doi.org/10.1175/1520-0469(2002)059<2729:ATCFTC>2.0.CO;2).
- Guo, H., Y. Liu, P. H. Daum, G. I. Senum, and W.-K. Tao, 2008: Characteristics of vertical velocity in marine stratocumulus: Comparison of large eddy simulations with observations. *Environ. Res. Lett.*, **3**, 045020, <https://doi.org/10.1088/1748-9326/3/4/045020>.
- Guo, Z., and Coauthors, 2015: Parametric behaviors of CLUBB in simulations of low clouds in the Community Atmosphere Model (CAM). *J. Adv. Model. Earth Syst.*, **7**, 1005–1025, <https://doi.org/10.1002/2014MS000405>.
- Gustafson, W. I., Jr., A. M. Vogelmann, X. Cheng, S. Endo, B. Krishna, Z. Li, T. Toto, and H. Xiao, 2017: Description of the LASSO Alpha 1 Release. DOE Office of Science ARM Program Tech. Rep. DOE/SC-ARM-TR-194, 46 pp., <https://doi.org/10.2172/1373564>.
- Hogan, R. J., A. L. M. Grant, A. J. Illingworth, G. N. Pearson, and E. J. O'Connor, 2009: Vertical velocity variance and skewness in clear and cloud-topped boundary layers as revealed by Doppler lidar. *Quart. J. Roy. Meteor. Soc.*, **135**, 635–643, <https://doi.org/10.1002/qj.413>.
- Holland, J. Z., and E. M. Rasmusson, 1973: Measurements of the atmospheric mass, energy, and momentum budgets over a 500-kilometer square of tropical ocean. *Mon. Wea. Rev.*, **101**, 44–55, [https://doi.org/10.1175/1520-0493\(1973\)101<0044:MOTAME>2.3.CO;2](https://doi.org/10.1175/1520-0493(1973)101<0044:MOTAME>2.3.CO;2).
- Ilyushin, B. B., and A. F. Kurbatskii, 1997: Modeling of turbulent transport in PBL with third-order moments. *Eleventh Symposium on Turbulent Shear Flows*, Vol. 2, Institut National Polytechnique de Grenoble, 2019–2021.
- Klemp, J. B., and R. B. Wilhelmson, 1978: The simulation of three-dimensional convective storm dynamics. *J. Atmos. Sci.*, **35**, 1070–1096, [https://doi.org/10.1175/1520-0469\(1978\)035<1070:TSOTDC>2.0.CO;2](https://doi.org/10.1175/1520-0469(1978)035<1070:TSOTDC>2.0.CO;2).
- Lappen, C.-L., and D. A. Randall, 2001: Toward a unified parameterization of the boundary layer and moist convection. Part I: A new type of mass-flux model. *J. Atmos. Sci.*, **58**, 2021–2036, [https://doi.org/10.1175/1520-0469\(2001\)058<2021:TAUPOT>2.0.CO;2](https://doi.org/10.1175/1520-0469(2001)058<2021:TAUPOT>2.0.CO;2).

- Larson, V. E., and J.-C. Golaz, 2005: Using probability density functions to derive consistent closure relationships among higher-order moments. *Mon. Wea. Rev.*, **133**, 1023–1042, <https://doi.org/10.1175/MWR2902.1>.
- , —, and W. R. Cotton, 2002: Small-scale and mesoscale variability in cloudy boundary layers: Joint probability density functions. *J. Atmos. Sci.*, **59**, 3519–3539, [https://doi.org/10.1175/1520-0469\(2002\)059<3519:SSAMVI>2.0.CO;2](https://doi.org/10.1175/1520-0469(2002)059<3519:SSAMVI>2.0.CO;2).
- Lenschow, D. H., M. Lothon, S. D. Mayor, P. P. Sullivan, and G. Canut, 2012: A comparison of higher-order vertical velocity moments in the convective boundary layer from lidar with in situ measurements and large-eddy simulation. *Bound.-Layer Meteor.*, **143**, 107–123, <https://doi.org/10.1007/s10546-011-9615-3>.
- Lewellen, W. S., and S. Yoh, 1993: Binormal model of ensemble partial cloudiness. *J. Atmos. Sci.*, **50**, 1228–1237, [https://doi.org/10.1175/1520-0469\(1993\)050<1228:BMOEPC>2.0.CO;2](https://doi.org/10.1175/1520-0469(1993)050<1228:BMOEPC>2.0.CO;2).
- Liu, L., F. Hu, and X.-L. Cheng, 2011: Probability density functions of turbulent velocity and temperature fluctuations in the unstable atmospheric surface layer. *J. Geophys. Res.*, **116**, D12117, <https://doi.org/10.1029/2010JD015503>.
- Lohmann, U., J. Feichter, C. C. Chuang, and J. E. Penner, 1999: Prediction of the number of cloud droplets in the ECHAM GCM. *J. Geophys. Res.*, **104**, 9169–9198, <https://doi.org/10.1029/1999JD900046>.
- Luhar, A. K., M. F. Hibberd, and P. J. Hurley, 1996: Comparison of closure schemes used to specify the velocity PDF in Lagrangian stochastic dispersion models for convective conditions. *Atmos. Environ.*, **30**, 1407–1418, [https://doi.org/10.1016/1352-2310\(95\)00464-5](https://doi.org/10.1016/1352-2310(95)00464-5).
- Maurer, V., N. Kalthoff, A. Wieser, M. Kohler, M. Mauder, and L. Gantner, 2016: Observed spatiotemporal variability of boundary-layer turbulence over flat, heterogeneous terrain. *Atmos. Chem. Phys.*, **16**, 1377–1400, <https://doi.org/10.5194/acp-16-1377-2016>.
- Mellor, G. L., 1977: The Gaussian cloud model relations. *J. Atmos. Sci.*, **34**, 356–358, [https://doi.org/10.1175/1520-0469\(1977\)034<0356:TGCMR>2.0.CO;2](https://doi.org/10.1175/1520-0469(1977)034<0356:TGCMR>2.0.CO;2).
- Millionshchikov, M. D., 1941: On the theory of homogeneous isotropic turbulence. *Dokl. Akad. Nauk SSSR*, **32**, 611–614.
- Moeng, C.-H., and D. A. Randall, 1984: Problems in simulating the stratocumulus-topped boundary layer with a third-order closure model. *J. Atmos. Sci.*, **41**, 1588–1600, [https://doi.org/10.1175/1520-0469\(1984\)041<1588:PISTST>2.0.CO;2](https://doi.org/10.1175/1520-0469(1984)041<1588:PISTST>2.0.CO;2).
- , and R. Rotunno, 1990: Vertical-velocity skewness in the buoyancy-driven boundary layer. *J. Atmos. Sci.*, **47**, 1149–1162, [https://doi.org/10.1175/1520-0469\(1990\)047<1149:VVSITB>2.0.CO;2](https://doi.org/10.1175/1520-0469(1990)047<1149:VVSITB>2.0.CO;2).
- Mole, N., and E. D. Clarke, 1995: Relationships between higher moments of concentration and of dose in turbulent dispersion. *Bound.-Layer Meteor.*, **73**, 35–52, <https://doi.org/10.1007/BF00708929>.
- Monin, A. S., and A. M. Yaglom, 1971: *Statistical Fluid Dynamics: Mechanics of Turbulence*. Vol. I, MIT Press, 769 pp.
- , and —, 1975: *Statistical Fluid Dynamics: Mechanics of Turbulence*. Vol. II, MIT Press, 874 pp.
- Morrison, H., G. Thompson, and V. Tatarskii, 2009: Impact of cloud microphysics on the development of trailing stratiform precipitation in a simulated squall line: Comparison of one- and two-moment schemes. *Mon. Wea. Rev.*, **137**, 991–1007, <https://doi.org/10.1175/2008MWR2556.1>.
- Moyer, K. A., and G. S. Young, 1991: Observations of vertical velocity skewness within the marine stratocumulus-topped boundary layer. *J. Atmos. Sci.*, **48**, 403–410, [https://doi.org/10.1175/1520-0469\(1991\)048<0403:OOVSW>2.0.CO;2](https://doi.org/10.1175/1520-0469(1991)048<0403:OOVSW>2.0.CO;2).
- Perraud, E., F. Couvreux, S. Malardel, C. Lac, V. Masson, and O. Thouron, 2011: Evaluation of statistical distributions for the parametrization of subgrid boundary-layer clouds. *Bound.-Layer Meteor.*, **140**, 263–294, <https://doi.org/10.1007/s10546-011-9607-3>.
- Quintarelli, F., 1990: A study of vertical velocity distributions in the planetary boundary layer. *Bound.-Layer Meteor.*, **52**, 209–219, <https://doi.org/10.1007/BF00122086>.
- Randall, D. A., 1987: Turbulent fluxes of liquid water and buoyancy in partly cloudy layers. *J. Atmos. Sci.*, **44**, 850–858, [https://doi.org/10.1175/1520-0469\(1987\)044<0850:TFOLWA>2.0.CO;2](https://doi.org/10.1175/1520-0469(1987)044<0850:TFOLWA>2.0.CO;2).
- , Q. Shao, and C.-H. Moeng, 1992: A second-order bulk boundary-layer model. *J. Atmos. Sci.*, **49**, 1903–1923, [https://doi.org/10.1175/1520-0469\(1992\)049<1903:ASOBBL>2.0.CO;2](https://doi.org/10.1175/1520-0469(1992)049<1903:ASOBBL>2.0.CO;2).
- Rauber, R. M., and Coauthors, 2007: Rain in Shallow Cumulus over the Ocean: The RICO campaign. *Bull. Amer. Meteor. Soc.*, **88**, 1912–1928, <https://doi.org/10.1175/BAMS-88-12-1912>.
- Shohat, J. A., and J. D. Tamarkin, 1943: *The Problem of Moments*. American Mathematical Society, 140 pp.
- Siebesma, A. P., and Coauthors, 2003: A large eddy simulation intercomparison study of shallow cumulus convection. *J. Atmos. Sci.*, **60**, 1201–1219, [https://doi.org/10.1175/1520-0469\(2003\)60<1201:ALESIS>2.0.CO;2](https://doi.org/10.1175/1520-0469(2003)60<1201:ALESIS>2.0.CO;2).
- Sommeria, G., and J. W. Deardorff, 1977: Subgrid-scale condensation in models of nonprecipitating clouds. *J. Atmos. Sci.*, **34**, 344–355, [https://doi.org/10.1175/1520-0469\(1977\)034<0344:SSCIMO>2.0.CO;2](https://doi.org/10.1175/1520-0469(1977)034<0344:SSCIMO>2.0.CO;2).
- Stevens, B., and Coauthors, 2003: Dynamics and Chemistry of Marine Stratocumulus—DYCOMS-II. *Bull. Amer. Meteor. Soc.*, **84**, 579–594, <https://doi.org/10.1175/BAMS-84-5-Stevens>.
- , and Coauthors, 2005: Evaluation of large-eddy simulations via observations of nocturnal marine stratocumulus. *Mon. Wea. Rev.*, **133**, 1443–1462, <https://doi.org/10.1175/MWR2930.1>.
- Tampieri, F., A. Maurizi, and S. Alberghi, 2000: Lagrangian models of turbulent dispersion in the atmospheric boundary layer. *Ingegneria del Vento in Italia 2000*, G. Solari, L. C. Pagnini, and G. Piccardo, Eds., National Association for Wind Engineering, 37–50.
- Tonttila, J., H. Järvinen, and P. Räisänen, 2015: Explicit representation of subgrid variability in cloud microphysics yields weaker aerosol indirect effect in the ECHAM5-HAM2 climate model. *Atmos. Chem. Phys.*, **15**, 703–714, <https://doi.org/10.5194/acp-15-703-2015>.
- VanZanten, M. C., and Coauthors, 2011: Controls on precipitation and cloudiness in simulations of trade-wind cumulus as observed during RICO. *J. Adv. Model. Earth Syst.*, **3**, M06001, <https://doi.org/10.1029/2011MS000056>.
- Waggy, S. B., A. Hsieh, and S. Biringen, 2016: Modeling high-order statistics in the turbulent Ekman layer. *Geophys. Astrophys. Fluid Dyn.*, **110**, 391–408, <https://doi.org/10.1080/03091929.2016.1196202>.
- Xiao, H., and Coauthors, 2015: Modifications to WRF's dynamical core to improve the treatment of moisture for large-eddy simulations. *J. Adv. Model. Earth Syst.*, **7**, 1627–1642, <https://doi.org/10.1002/2015MS000532>.
- Yamaguchi, T., and G. Feingold, 2012: Large-eddy simulation of cloudy boundary layer with the Advanced Research WRF model. *J. Adv. Model. Earth Syst.*, **4**, M09003, <https://doi.org/10.1029/2012MS000164>.
- Zhu, P., and P. Zuidema, 2009: On the use of PDF schemes to parameterize sub-grid clouds. *Geophys. Res. Lett.*, **36**, L05807, <https://doi.org/10.1029/2008GL036817>.